

## Mapping the Earth's thermochemical and anisotropic structure using global surface wave data

A. Khan,<sup>1,2</sup> L. Boschi,<sup>3</sup> and J. A. D. Connolly<sup>4</sup>

Received 6 July 2010; revised 24 September 2010; accepted 11 October 2010; published 5 January 2011.

[1] We have inverted global fundamental mode and higher-order Love and Rayleigh wave dispersion data jointly, to find global maps of temperature, composition, and radial seismic anisotropy of the Earth's mantle as well as their uncertainties via a stochastic sampling-based approach. We apply a self-consistent thermodynamic method to systematically compute phase equilibria and physical properties ( $P$  and  $S$  wave velocity, density) that depend only on composition (in the  $\text{Na}_2\text{-CaO-FeO-MgO-Al}_2\text{O}_3\text{-SiO}_2$  model system), pressure, and temperature. Our 3-D maps are defined horizontally by 27 different tectonic regions and vertically by a number of layers. We find thermochemical differences between oceans and continents to extend down to  $\sim 250$  km depth, with continents and cratons appearing chemically depleted (high magnesium number (Mg #) and Mg/Si ratio) and colder ( $>100^\circ\text{C}$ ) relative to oceans, while young oceanic lithosphere is hotter than its intermediate age and old counterparts. We find what appears to be strong radial  $S$  wave anisotropy in the upper mantle down to  $\sim 200$  km, while there seems to be little evidence for shear anisotropy at greater depths. At and beneath the transition zone, 3-D heterogeneity is likely uncorrelated with surface tectonics; as a result, our tectonics-based parameterization is tenuous. Despite this weakness, constraints on the gross average thermochemical and anisotropic structure to  $\sim 1300$  km depth can be inferred, which appear to indicate that the compositions of the upper (low Mg# and high Mg/Si ratio) and lower mantle (high Mg# and low Mg/Si ratio) might possibly be distinct.

**Citation:** Khan, A., L. Boschi, and J. A. D. Connolly (2011), Mapping the Earth's thermochemical and anisotropic structure using global surface wave data, *J. Geophys. Res.*, 116, B01301, doi:10.1029/2010JB007828.

### 1. Introduction

[2] Since its infancy in the late 1970s and early 1980s, seismic tomography [e.g., *Dziewonski et al.*, 1977; *Woodhouse and Dziewonski*, 1984; *Dziewonski*, 1984] has become a well-established discipline that has done much to enhance our understanding of deep Earth processes, providing detailed information on the large-scale velocity variations that pervade the mantle. In particular, the last decade has seen a growing level of consensus where studies employing different data sets and/or forward or inverse modeling techniques are converging toward a consistent picture of the long wavelength pattern of elastic wave speeds (see reviews and model comparisons by, e.g., *Nolet et al.* [1994],

*Montagner* [1994], *Ritzwoller and Lavelly* [1995], *Trampert and Woodhouse* [2001], *Becker and Boschi* [2002], *Romanowicz* [2003], *Trampert and van der Hilst* [2005], and *Rawlinson et al.* [2010]).

[3] In spite of the success of seismic tomography in elucidating the physical structure (seismic  $P$  and  $S$  wave speeds) of the mantle, knowledge of seismic wave velocities is not an end in itself as it only provides clues about the underlying processes that determine the evolution of the mantle, i.e., chemical makeup and thermal state.

[4] The case for compositional heterogeneity playing a major role has steadily increased in significance over recent years. Analyses of the ratio of relative changes in shear and compressional wave velocities ( $V_S$  and  $V_P$ , respectively), defined as  $R_{P/S} = \partial \ln V_S / \partial \ln V_P$ , have been inferred from seismic tomography studies and been given ample consideration as a possible means to unravel the physical causes of the observed velocity variations [e.g., *Robertson and Woodhouse*, 1996; *Su and Dziewonski*, 1997; *Masters et al.*, 2000; *Saltzer et al.*, 2001; *Romanowicz*, 2001; *Resovsky and Trampert*, 2003; *Simmons et al.*, 2009]. From the aforementioned studies it is generally agreed that  $R_{P/S}$  increases radially, although important lateral variations are also acknowledged to exist. However, more often than not, independent overlapping information on  $P$  and  $S$  wave

<sup>1</sup>Niels Bohr Institute, University of Copenhagen, Denmark.

<sup>2</sup>Now at Institute of Geochemistry and Petrology and Institute of Geophysics, Swiss Federal Institute of Technology, Zurich, Switzerland.

<sup>3</sup>Institute of Geophysics, Swiss Federal Institute of Technology, Zurich, Switzerland.

<sup>4</sup>Institute of Geochemistry and Petrology, Swiss Federal Institute of Technology, Zurich, Switzerland.

velocities is not available and, even in cases where it is, *Deschamps and Trampert* [2003] have shown that  $R_{P/S}$  can only give a qualitative indication of chemical variations.

[5] Recent advances in seismic tomography and mineral physics, particularly knowledge of the elastic properties of mantle phases at high pressure and temperature, have spurred an increased interest in the origins of the observed lateral variations in physical properties of mantle and crustal materials. More importantly, the mineral physics database has now reached a level of maturity enabling quantitative inferences to be drawn about the underlying nature of the processes that produce the observed variations in seismic wave speeds [e.g., *Trampert and van der Hilst*, 2005]. As a result, some recent studies have attempted to infer thermochemical variations in the mantle directly by combining geophysical models and data with mineral physics databases. These studies [e.g., *Jackson*, 1998; *Goes et al.*, 2000; *Deschamps and Trampert*, 2004; *Trampert et al.*, 2004; *Cammarano et al.*, 2009; *Khan et al.*, 2009; *Afonso et al.*, 2008; *Verhoeven et al.*, 2009; *Cobden et al.*, 2009] found significant spatially varying departures in temperature and composition from the standard adiabatic pyrolite model of *Ringwood* [1975], superseding analyses where seismic velocity variations are interpreted as having a purely thermal origin [e.g., *Cammarano and Romanowicz*, 2007; *Ritsema et al.*, 2009; *Simmons et al.*, 2009], and call for a revision of mantle flow calculations based on simple positive scaling relationships between seismic wave speeds and density [e.g., *Forté and Perry*, 2000; *Forté and Mitrovica*, 2001].

[6] Although seismic tomography continues to produce spectacular images of Earth's mantle, these images generally lack a careful analysis of model resolution and uncertainty. These points, which are integral parts of any study seeking to make quantitative inferences from inverse calculations, have, however, generally not been accorded the same attention as the quest for increased lateral resolution of imaged velocity variations. Seismic tomography is typically based on linearized inversion algorithms, resulting in images of the Earth that tend to be biased toward the particular starting model and regularization scheme chosen. As a result, quantifying uniqueness, accuracy, and resolution of tomographic models becomes complicated to the point that tomography models are presented as a *fait accompli*, with no quantitative assessment of their overall reliability [e.g., *Trampert*, 1998; *Boschi and Dziewonski*, 1999; *Shapiro and Ritzwoller*, 2002; *Trampert and van der Hilst*, 2005].

[7] With this in mind, the purpose of the present study is twofold: (1) to map the global compositional and thermal structure of the Earth's mantle as well as anisotropy using global surface wave data and (2) to employ a stochastic sampling-based algorithm to solve the nonlinear inverse problem, thereby consigning regularization and other related ills to oblivion. Stochastic approaches based on Markov chain Monte Carlo (MCMC) methods have become increasingly popular in geophysics because of their versatility and ability to provide quantitative measures of model resolution, uncertainty, and nonuniqueness [e.g., *Mosegaard and Sambridge*, 2002; *Sambridge and Mosegaard*, 2002, and references therein]. This has been less the case in the field of seismic tomography, mainly because of the large number of parameters that are sought in the latter and the

computationally intensive nature of MCMC methods, although the studies of *Shapiro and Ritzwoller* [2002], *Visser et al.* [2008a], and *Khan et al.* [2009] present a change in direction along the lines sought here.

[8] Because of present-day computational limitations it is impractical to attempt to achieve resolution on a global scale of  $<20^\circ$  using MCMC methods. As a consequence, we employ an extended version of the global tectonic regionalization scheme of *Jordan* [1981], which consisted of six different tectonic regions (three for the oceans and three for the continents). Here we extend the map to encompass 27 different regions (three for each continent and major ocean, respectively). A parameterization based on tectonic regionalization will describe adequately the lateral structure of the upper mantle; at larger depths, however, the large-scale pattern of heterogeneity is less likely to follow a tectonic pattern. The regionalization approach to seismic tomography is not new and has previously been applied by, for example, *Nataf and Ricard* [1996] and *Gudmundsson and Sambridge* [1998]. The latter authors, for example, constructed a regionalized upper mantle  $P$  and  $S$  wave velocity model for eight different tectonic provinces using global travel times.

[9] As in our previous study [*Khan et al.*, 2009], we base ourselves on the global surface wave data set of *Visser et al.* [2008a], which consists of Love and Rayleigh wave phase velocities from fundamental modes and overtones (up to fifth (Love) and sixth (Rayleigh) order, respectively). In our previous study we inverted local dispersion curves taken at selected points on the globe. Here we first calculate average dispersion curves, for each of the 27 tectonic regions, from *Visser et al.*'s phase-velocity maps, and then invert each of the 27 curves separately.

[10] To understand the nature of seismic velocity variations, we invert seismic data directly for the thermochemical state and anisotropic structure of the Earth's mantle. In this we follow the approach of our previous study [*Khan et al.*, 2009], where we employed a self-consistent thermodynamic method to compute mineral phase equilibria and associated seismic  $P$  and  $S$  wave velocities as well as density that depend only on composition, temperature, and pressure (depth). More physically realistic models are obtained as a result, including a natural scaling between  $P$  and  $S$  wave velocities on the one hand and density on the other. Moreover, since pressure-induced mineralogical phase changes depend on the particular composition and physical conditions of a given model, the size and location (depth) of the associated change in physical properties respond naturally to the particular conditions of interest.

[11] The importance of considering anisotropy stems from the constraints that it provides on mantle flow as anisotropy likely reflects present-day mantle strain field or past deformation frozen in the lithosphere [e.g., *Tanimoto and Anderson*, 1984; *Karato*, 1998; *Montagner*, 1998; *Becker et al.*, 2008]. As a consequence, seismic anisotropy has figured prominently in tomographic studies, although there currently is little consensus surrounding the presence of  $S$  wave anisotropy other than in the upper mantle.

[12] In summary, our goals are (1) to detail robust, long wavelength features of seismic models, including ocean-continent differences and their depth extent, and anisotropy in and below the TZ and (2) to establish the degree to which

mantle composition and temperature can be constrained independently of each other.

## 2. Tectonic Regionalization and Surface Wave Dispersion Data

[13] The scheme for partitioning the surface of the Earth laterally is based on the global tectonic regionalization scheme (GTR1) of *Jordan* [1981], which consisted of 6 major divisions: three for the oceans (young, intermediate age, and old ocean) and three for the continents (shields and platforms of exposed Archean and Proterozoic rocks, platforms overlain by relatively undisturbed Phanerozoic cover, and Phanerozoic orogenic zones and magmatic belts). In the present study we simply extended the original GTR1 map so that all major oceans (Pacific, Atlantic, and Indian) and continents (North America, South America, Eurasia, Africa, Australia, and Antarctica) are described by three different pixels each amounting to 27 different regions in all. The tectonic map so produced is shown in Figure 1 on a  $5^\circ \times 5^\circ$  grid.

[14] The premise behind GTR1 as discussed by *Jordan* [1981] is that the large-scale heterogeneity of the upper mantle is essentially caused by variations in the structure and thickness of the tectosphere. For this reason the parameterization adopted here should be appropriate for describing the upper mantle, whereas for deeper regions the adequacy of this approach is less obvious. However, on the basis of current tomographic maps of seismic  $P$  and  $S$  wave speeds, which show amplitudes of heterogeneities to decrease from a maximum in the uppermost upper mantle down through the TZ and into the midmantle region, it is expected that the tectonic regionalization will appear less prominent (smoothed out) as the TZ is approached. Other prominent features of tomography models in and below the TZ are velocity contrasts associated with subduction zones and signatures of slabs. However, as the tectonic regionalization scheme employed here averages relatively large areas, any such features inherent in the original data are smoothed out.

[15] Our data set consists of the global azimuthal anisotropic phase-velocity maps of fundamental and higher-mode Love (up to fifth order) and Rayleigh (up to sixth order) waves of *Visser et al.* [2008a] and represents the isotropic part (azimuthally averaged) of their phase-velocity maps. The maps were obtained after first performing a linear inversion of their global phase delay database. The lateral resolution of *Visser et al.*'s maps is  $5^\circ \times 5^\circ$ . The sensitivity of these waves is partitioned as follows: the fundamental mode senses mostly the upper mantle, while higher modes have increased sensitivity at depth such that these modes sense the TZ and upper part of the lower mantle down to  $\sim 1300$  km depth. Importantly, while fundamental mode surface waves are predominantly sensitive to horizontally and vertically polarized  $S$  wave velocity, the relative sensitivity of higher modes to compressional velocity (for Rayleigh waves) and density grows with increasing overtone number [see *Anderson and Dziewonski*, 1982]. It is precisely the fact that individual surface wave modes have different sensitivity to density and shear and compressional velocity that allows us to determine both thermal and compositional structure from a joint inversion of these data.

[16] For each of the 27 different tectonic regions, for example for all pixels labeled "a" and corresponding to young Pacific ocean, we extracted Love and Rayleigh wave dispersion curves from *Visser et al.*'s [2008a] global phase velocity maps and then averaged these over all "a" pixels. The average Love and Rayleigh wave dispersion curves for all pixels of a given tectonic region, then, make up our regional data set, with the one standard deviation computed from the spread, which is used as a measure of data uncertainty. For each tectonic region, we thus have 13 dispersion curves consisting of a total of 149 distinct Love and Rayleigh wave phase velocities as a function of frequency, which we invert jointly for regional compositional, thermal, and radial anisotropic structure. Examples of regional dispersion curves are shown in section 5.1.

[17] The database of *Visser et al.* [2008a] represents an important, original contribution to efforts in mantle imaging; it consists of a comprehensive compilation of surface wave dispersion observations including overtones, capable of providing much higher resolution of upper mantle and uppermost lower mantle structure than what can be achieved by simple body wave or fundamental mode surface wave inversions.

## 3. The Forward Problem

### 3.1. Constructing the Forward Problem

[18] The parameterization governing lateral variations in properties is shown in Figure 1. In the radial direction, we consider properties to vary in a prescribed set of layers of variable thickness, corresponding to crust, upper mantle, TZ, and lower mantle. Model parameters pertinent to these layers are the (1) physical structure of the crust, (2) composition, (3) temperature, (4) anisotropy, (5) seismic wave attenuation (mantle), and (6) layer thickness (the parameters are discussed in detail in section 3.2).

[19] To compute Love and Rayleigh wave dispersion curves ( $C_L(\omega)$  and  $C_R(\omega)$ ) from the model parameters mentioned earlier, we need to set up and solve the forward problem  $\mathbf{d} = \mathbf{g}(\mathbf{m})$ , where  $\mathbf{m}$  are the model parameters,  $\mathbf{d}$  are data, and  $\mathbf{g}$  comprises the physical law(s) that connect model parameters and data. Following our previous approach [*Khan et al.*, 2009], we summarize the forward problem in Figure 2, where  $c$  and  $T$  denote composition and temperature, respectively;  $M$  are mineral phase proportions (modal mineralogy);  $V_p$ ,  $V_s$ , and  $\rho$  are  $P$  and  $S$  wave velocities and density, respectively;  $\xi$ ,  $\phi$ , and  $\eta$  are anisotropy parameters (defined in section 3.2),  $Q$  is the attenuation structure; and  $V_{sv}$ ,  $V_{sh}$ ,  $V_{pv}$ , and  $V_{ph}$  are the velocities of vertically (v) and horizontally (h) polarized  $S$  waves and vertically and horizontally propagating  $P$  waves, respectively. All parameters are implicitly assumed to be functions of radius. The  $g$ 's comprise the physical laws, where  $g_1$  embodies the Gibbs free energy minimization routine, which calculates modal mineralogy;  $g_2$  estimates bulk isotropic physical properties;  $g_3$  determines anelastic and anisotropic properties; and  $g_4$  computes Love and Rayleigh wave dispersion curves.

[20] The pressure profile is needed to compute mineralogical structure and mass density, which is obtained by integrating the load from the surface (boundary condition  $p = 10^5$  Pa). The following sections briefly delineate the physical connections, while model parameters are revisited in section 4.2.

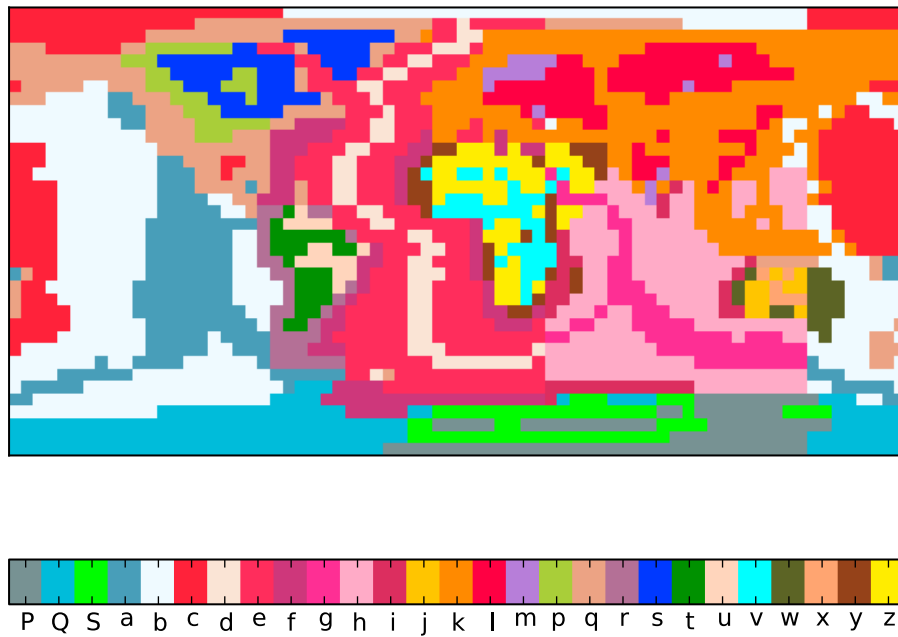


**Figure 1.** A  $5^\circ \times 5^\circ$  geographic grid showing the generalized tectonic regions making up our map, which is based on the original GTR1 map of *Jordan* [1981]. The three major oceans are partitioned into three age regions (young, intermediate, and old). Continental crustal division is based on crustal tectonic history during the Phanerozoic. Divisions are Precambrian shields and platforms, Phanerozoic platforms, and Phanerozoic orogenic zones and magmatic belts.

### 3.2. Gibbs Free Energy Minimization

[21] We assume mantle mineralogy is dictated by thermodynamic equilibrium and predict this mineralogy as a function of local composition, pressure, and temperature by Gibbs energy minimization using the method of *Connolly* [2005]. For this purpose we adopt the thermodynamic formalism of *Stixrude and Lithgow-Bertelloni* [2005] as parameterized by *Xu et al.* [2008] for mantle minerals in the model chemical system  $\text{Na}_2\text{O}-\text{CaO}-\text{FeO}-\text{MgO}-\text{Al}_2\text{O}_3-\text{SiO}_2$  (abbreviated NCFMAS). The Gibbs energy minimization procedure yields the amounts, compositions, and physical properties, including elastic moduli, of the stable minerals in the model chemical system. Aggregate elastic moduli are estimated from this information by Voigt-Reuss-Hill averaging.

[22] As an alternative to the aforementioned equilibrium model, *Xu et al.* [2008] recently proposed the mechanical mixture model. This model represents the extreme scenario in which pyrolitic mantle has undergone complete differentiation to basaltic and harzburgitic rocks and bulk prop-

erties are computed by averaging the properties of the minerals in the basaltic and harzburgitic end members. In contrast, the equilibrium model assumes that harzburgitic and basaltic components are chemically equilibrated and bulk properties are computed from the mineralogy obtained by free energy minimization for the resulting bulk composition. However, from a petrological perspective, a fully segregated model for the Earth's mantle is undesirable because it is inconsistent with basaltic volcanism at mid-ocean ridges.

### 3.3. Anelasticity

[23] It has been argued that effects arising from the viscoelastic behavior of materials at elevated temperatures (i.e., attenuation and dispersion) could be potentially important in the interpretation of seismic velocities in tomography images [*Karato*, 1993; *Matas and Bukowinski*, 2007; *Brodholt et al.*, 2007]. Traditionally, global 1-D models of attenuation ( $Q$ ) have been obtained from the analysis of surface wave and normal mode data [e.g., *Anderson and Hart*,

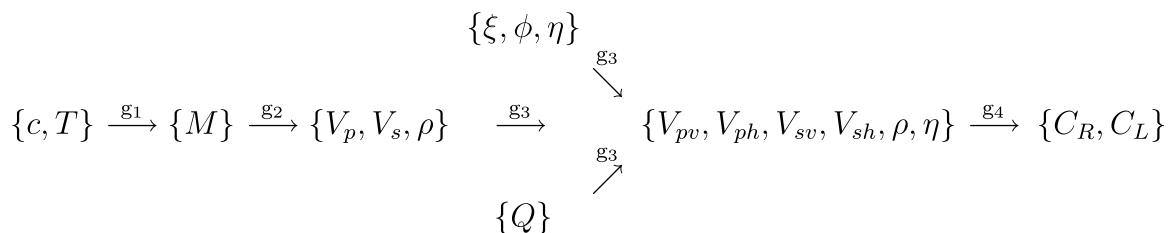


**Figure 2.** A schematic illustration of the forward problem and the different model parameters ( $c$ ,  $T$ ,  $\xi$ ,  $\phi$ , ...), physical theories ( $g_1$ ,  $g_2$ , ...), and data ( $C_R$ ,  $C_L$ ) used to enumerate it. Symbols are described in section 3.1.

1978; *Dziewonski and Anderson*, 1981; *Widmer et al.*, 1991; *Durek and Ekström*, 1996], as well as differential attenuation measurements of  $S$  and  $ScS$  phases [*Lawrence and Wyssession*, 2006]. From an experimental point of view, attenuation has been found to be strongly temperature-dependent and in the case of shear (bulk attenuation is assumed to be less significant with values in the range  $\sim 10^3$ – $10^4$  [*Durek and Ekström*, 1996]) to follow an Arrhenius-type law of the form [e.g., *Anderson*, 1989; *Karato*, 1993; *Jackson*, 2000]

$$Q_\mu = Q_0 \exp \left[ \frac{\alpha(E_a + pV_a)}{RT} \right], \quad (1)$$

where  $Q_0$  is a constant,  $E_a$  is the activation energy,  $V_a$  is the activation volume,  $p$  is pressure,  $T$  is temperature,  $R$  is the gas constant, and  $\alpha$  is an exponent. The latter has been determined experimentally to be in the range 0.15–0.25 [*Jackson et al.*, 2002] and in the range 0.1–0.4 theoretically [*Minster and Anderson*, 1981]. That  $Q$  is weakly frequency dependent throughout most of the mantle is in line with the absorption band model, where attenuation is modeled as arising from a broad distribution of thermally activated relaxation processes [e.g., *Kanamori and Anderson*, 1977; *Minster and Anderson*, 1981; *Anderson and Given*, 1982].

[24] A consequence of a dissipative system is the presence of velocity dispersion due to attenuation. Given a model of  $Q_\mu$  ( $= Q_s$ ) and assuming a weakly frequency-dependent  $Q$  ( $Q \propto \omega^\alpha$ ,  $0 < \alpha < 1$  [*Karato and Spetzler*, 1990]), anelastic shear velocities  $V$  are determined according to the model of *Minster and Anderson* [1981]:

$$V_s(p, T, c) = v_s(p, T, c) \left[ 1 - \frac{2Q_s^{-1}}{\tan(\alpha\pi/2)} \right], \quad (2)$$

where  $v_s$  is the isotropic anharmonic  $S$  wave velocity as a function of  $p$ ,  $T$ , and composition  $c$ , obtained using Gibbs free energy minimization.  $P$  wave velocities are obtained by replacing  $Q_s^{-1}$  by  $Q_p^{-1} = (4V_s^2/3V_p^2)Q_\mu^{-1}$ , where contributions from bulk attenuation  $Q_\kappa$  have been disregarded (typically  $Q_\kappa \rightarrow \infty$  [*Romanowicz and Mitchell*, 2007]).

### 3.4. Anisotropy

[25] As in most surface wave tomography studies [e.g., *Panning and Romanowicz*, 2006; *Kustowski et al.*, 2008], we assume transverse anisotropy (symmetry axis in vertical direction), in which case the number of independent unknowns needed to describe the system is five. For present purposes it is of advantage to work with  $V_{sv}$ ,  $V_{sh}$ ,  $V_{pv}$ , and  $V_{ph}$ , as defined in section 3.1. We introduce the three anisotropy parameters  $\xi$ ,  $\phi$ , and  $\eta$ , which are related to  $V_{sv}$ ,  $V_{sh}$ ,  $V_{pv}$ , and  $V_{ph}$  through

$$\xi = \frac{V_{sh}^2}{V_{sv}^2}, \quad \phi = \frac{V_{pv}^2}{V_{ph}^2}, \quad \eta = \frac{F}{A - 2L}, \quad (3)$$

where  $\xi$  and  $\phi$  quantify  $S$  and  $P$  wave anisotropy, respectively;  $\eta$  describes the dependence of velocity on the incidence angle of a propagating wave [*Dziewonski and Anderson*, 1981; *Anderson and Dziewonski*, 1982]; and  $F$ ,  $A$ , and  $L$  are three of the Love coefficients. Reparameteriz-

ing in terms of the Voigt average of isotropic  $P$  and  $S$  wave velocities [*Babuska and Cara*, 1991],

$$V_p^2 = \frac{V_{pv}^2 + 4V_{ph}^2}{5}, \quad (4)$$

$$V_s^2 = \frac{2V_{sv}^2 + V_{sh}^2}{3}, \quad (5)$$

where  $V_s^2$  and  $V_p^2$  are isotropic (anelastically corrected)  $P$  and  $S$  wave velocities, respectively.

[26] In summary, from the set of parameters  $\{V_p, V_s, \xi, \phi, \eta\}$ , anisotropic velocities are computed using equations (3)–(5), which are subsequently employed to determine Love and Rayleigh wave dispersion curves. Note that because we are employing surface wave overtone data we are sensitive not only to  $S$  wave velocity but also to  $P$  wave velocity, as discussed earlier.

## 4. The Inverse Problem

### 4.1. Formulation and Solution of the Inverse Problem

[27] One of the fundamental problems encountered when having to solve the general inverse problem  $\mathbf{d} = g(\mathbf{m})$ , where  $\mathbf{d}$  is a data vector and  $g$  a typically nonlinear operator that maps a model parameter vector  $\mathbf{m}$  into data, is the absence in mathematical terms of a closed analytical expression for evaluating  $\mathbf{d}$  for any given  $\mathbf{m}$ . Instead, what we have is a set of algorithms (forward modeling routines) that allow us to go from  $\mathbf{m}$  to  $\mathbf{d}$ . This case is excellently represented in Figure 2. A set of different routines is employed in order to estimate Rayleigh and Love wave dispersion curves from a knowledge of Earth's thermochemical state. As in our previous work we employ the probabilistic approach of *Tarantola and Valette* [1982] to solving the nonlinear inverse problem.

[28] Within the Bayesian framework, the solution to the general inverse problem is given by [e.g., *Tarantola and Valette*, 1982; *Mosegaard and Tarantola*, 1995]

$$\sigma(\mathbf{m}) = kf(\mathbf{m})\mathcal{L}(\mathbf{m}), \quad (6)$$

where  $k$  is a normalization constant;  $f(\mathbf{m})$  is the prior probability distribution on model parameters (i.e., information about model parameters obtained independently of data);  $\mathcal{L}(\mathbf{m})$  is the likelihood function, which in probabilistic terms can be interpreted as a measure of misfit between the observations and the predictions from model  $\mathbf{m}$ ; and  $\sigma(\mathbf{m})$  is the posterior model parameter distribution containing the solution to the inverse problem. The particular form of  $\mathcal{L}(\mathbf{m})$  is determined by the observations, their uncertainties, and how these are employed to model data noise. For further details we refer the reader to our previous work [e.g., *Khan et al.*, 2007, 2009].

### 4.2. Prior Information

#### 4.2.1. Crust

[29] Surface waves are sensitive to crustal structure and we employ CRUST2.0 as an initial starting model. CRUST2.0 is a global crustal model that specifies  $\rho$ ,  $V_p$ ,  $V_s$ , and Moho depth on a  $2^\circ \times 2^\circ$  grid (<http://mahi.ucsd.edu/Gabi/rem.html>). For each particular region we computed an

average four-layer crustal model from CRUST2.0 as a starting model. In each of the four layers,  $\rho$ ,  $V_p$ , and  $V_s$  are variable within upper and lower bounds, where the former are  $\rho = 1.5 \text{ g/cm}^3$ ,  $V_p = 2.5 \text{ km/s}$ , and  $V_s = 1.5 \text{ km/s}$  and the latter correspond to the thermodynamically determined parameter at the first node in the mantle, respectively. In addition, we assume  $\rho$ ,  $V_p$ , or  $V_s$  to be nondecreasing as a function of depth, while Moho depth  $d_{cr}$  is left variable to within  $\pm 5 \text{ km}$  (oceanic regions) and  $\pm 20 \text{ km}$  (continental regions) of the crustal thickness specified by the average model for each region extracted from CRUST2.0. This amounts to 13 parameters per tectonic region. (It is implicitly assumed in what follows that the number of parameters per tectonic region is implied.)

#### 4.2.2. Temperature

[30] In evaluating the temperature  $T$  in a given layer  $k$ , no lower or upper bounds are applied except for surface temperature, which is held constant at  $0^\circ\text{C}$ . We additionally employ the constraint  $T_{k-1} \leq T_k \leq T_{k+1}$ , i.e., temperatures cannot be decreasing as a function of depth. Using this scheme, we determine temperatures in 25 uniform layers at intervals of 50 km in the depth range 0–700 km, and 100 km in the range 700–2886 km, resulting in 26 parameters.

#### 4.2.3. Layer Thickness

[31] From a compositional point of view, we model the crust and mantle as consisting of four layers. The depths to these individual layer boundaries are variable, with crustal thickness specified above, while for the upper and lower mantle layer boundaries we assume these to be uniformly distributed within depth ranges 200–500 and 600–700 km, respectively. Earth's surface and core-mantle boundary are fixed at 6371 and 3480 km, respectively, in accordance with the preliminary Earth reference model (PREM). This corresponds to four parameters.

#### 4.2.4. Silicate Mantle Composition

[32] Mantle compositions were explored within the NCFMAS system, a model that accounts for more than 98% of the mass of the mantle [Irfune, 1994]. Mantle compositions  $c$  adopted here are assumed to be uniformly distributed in all three mantle layers within the bounds given in Table 1. The bounds chosen for the upper mantle are such that our compositions are in agreement with the range of compositions of mantle peridotites derived from several geochemical studies [see Lyubetskaya and Korenaga, 2007, Table 2], while a bit more leniency is left in the TZ and lower mantle, in particular with regard to the most important components, FeO, MgO, and SiO<sub>2</sub>, from the point of view of elastic properties. This results in 15 parameters.

#### 4.2.5. Attenuation and Anelasticity

[33] Because of the scarcity in laboratory measurements of these parameters for the appropriate minerals considered here and not least the few constraints that surface wave tomographic studies are able to provide on  $Q$ , we follow a standard procedure in the field and essentially remove  $Q$  from the list of variables. However, rather than fixing it to PREM, for example, we compute  $Q$  according to equation (1) by fixing  $E_a = 5 \times 10^2 \text{ kJ/mol}$ ,  $V_a = 2.5e^{-5} \text{ cm}^3/\text{mol}$ ,  $Q_0 = 1$ , and  $\alpha = 0.2$  [Sobolev et al., 1996; Cobden et al., 2008], while pressure  $p$  derives from the thermodynamic method and  $T$  is a model parameter. This ensures some variability in  $Q$  without leading to any major disturbance when computing anelastic velocities from equation (2).

#### 4.2.6. Anisotropy

[34] For the anisotropy parameters we use a parameterization where we assume  $\xi$ ,  $\phi$ , and  $\eta$  to be constant within a number of layers, with the following upper and lower layer boundaries: 0–25, 26–50, 51–100, 101–150, 151–250, 251–350, 351–450, 451–600, 601–800, 801–1000, 1001–1200, 1201–1400, 1401–1600, 1601–1800, and 1801–2000 km depth. We additionally assume  $\xi$ ,  $\phi$ , and  $\eta$  to be uniformly distributed within certain bounds (see Table 2). These bounds were chosen to bracket most of the range of values of recent anisotropy estimates obtained from surface wave tomography studies [e.g., Panning and Romanowicz, 2006; Kustowski et al., 2008; Visser et al., 2008b]. Note that these latter studies did not provide any constraints on  $\phi$  and  $\eta$ . This corresponds to 16 parameters.

#### 4.2.7. Isotropic and Anisotropic Physical Properties

[35] Isotropic physical properties ( $V_p$ ,  $V_s$ , and  $\rho$ ) and anisotropic physical properties ( $V_{sh}$ ,  $V_{sv}$ ,  $V_{ph}$ , and  $V_{pv}$ ) are secondary model parameters that depend on primary model parameters ( $c$  and  $T$  as well as pressure). Thus, no prior information on these parameters applies here.

#### 4.3. Sampling the Posterior

[36] In all, we have to determine 74 parameters for each tectonic region. For a set of values of these 74 model parameters, the thermodynamic model is used to establish equilibrium mineralogy, density, and physical properties of 65 crust and mantle layers (layer thickness is 10 km in the depth range 0–100 km; 30 km in the depth ranges 100–370, 420–540, and 570–630 km; 5 km in the depth ranges 370–420, 420–540, and 630–700 km; and 100 km at depths of 700 km and more) from the surface downward as a function of pressure, temperature, and composition. Once these values have been set up, Love and Rayleigh wave dispersion curves can be computed for each tectonic province.

[37] As in our previous study we model the likelihood function as

$$\mathcal{L}(\mathbf{m}) \propto \exp\left(-\sum_{\text{mode frequency}} \sum \frac{[d_{\text{obs}}^R - d_{\text{cal}}^R(\mathbf{m})]^2}{2\sigma_R^2} - \sum_{\text{mode frequency}} \sum \frac{[d_{\text{obs}}^L - d_{\text{cal}}^L(\mathbf{m})]^2}{2\sigma_L^2}\right),$$

where  $d_{\text{obs}}$  denotes observed data,  $d_{\text{cal}}(\mathbf{m})$  denotes calculated data, superscripts  $R$  and  $L$  denote Rayleigh and Love waves, respectively, and  $\sigma_{R,L}$  denotes uncertainty on either of these. Implicit in the form of the  $\mathcal{L}(\mathbf{m})$  is the assumption that data noise can be modeled using a Gaussian distribution and the independence of observational uncertainties and calculation errors between Rayleigh and Love waves.

[38] The number of iterations until convergence is reached and samples were retained from the posterior distribution (burn-in time) was  $\sim 10^4$  for our adopted distribution. In all, we sampled a million models and to ensure near-independent samples every 100th model was retained for analysis, with an overall acceptance rate of  $\sim 35\%$ .

[39] By the probabilistic nature of our approach the posterior distribution (equation (6)) is itself a probability density function (pdf), which in the case of nonlinear inverse problems is typically multimodal. This means that in

**Table 1.** Model Compositions

Component	Upper Mantle (wt %)	TZ (wt %)	Lower Mantle (wt %)
CaO	2.32–3.88	2.32–3.88	2.32–3.88
FeO	7.24–8.84	6–10	<sup>a</sup>
MgO	35–41.6	35–41.6	35–41.6
Al <sub>2</sub> O <sub>3</sub>	2.92–4.87	2.92–4.87	2.92–4.87
SiO <sub>2</sub>	40.5–49.4	<sup>a</sup>	40.5–49.4
Na <sub>2</sub> O	<sup>a</sup>	0.157–0.439	0.157–0.439

<sup>a</sup>Components determined by the constraint that all have to sum to 100 wt %.

addition to the global extremum corresponding to the most probable model, there are other secondary extrema implying other possible solutions. There are several ways to extract the information contained in the posterior pdf. The movie strategy advocated by *Mosegaard and Tarantola* [1995] is a strong tool for visually inspecting models and gives good insight into which features in the sampled models are well or ill resolved. However, this approach is less applicable here because we are interested in looking at global maps of various properties, and displaying  $\sim 100$  of them would take too much space. Given that  $\sigma(\mathbf{m})$  is a complicated function, it is more convenient, and probably also sufficient for general orientation regarding the uncertainty about  $\mathbf{m}$ , simply to describe regions of given probability under  $\sigma(\mathbf{m})$ . From this point of view the identification of intervals containing 50%, 90%, or 99% of the probability under  $\sigma(\mathbf{m})$  actually suffice to give a good idea of the general quantitative messages implicit in  $\sigma(\mathbf{m})$ . The most appropriate measures for this purpose are credible intervals, which are defined as the shortest possible interval containing a given probability [e.g., *Bernardo and Smith*, 1994]. In addition to displaying upper and lower 75% credible intervals for a given parameter, we also show the most probable model. However, we would like to emphasize that the most probable model is no more representative or credible than any other model taken randomly from the posterior pdf.

[40] In interpreting the results, we have to be aware of limitations imposed by our choice of model parameterization. Any inversion faces the trade-off problem between model parameter uncertainty and resolution. We made no exhaustive examination of the effect of different parameterizations; rather we have chosen one that results in data being fit within uncertainties. Preliminary investigations suggested that a simpler compositional parameterization (i.e., homogeneous mantle composition) had more difficulty in achieving the necessary level of data fit, although some tectonic regions could be fit reasonably well. At the other end of the scale, we also briefly investigated a parameterization with a larger number of compositional layers, which resulted in the requisite data fit but left mantle composition poorly constrained. In addition, we presently model chemical composition using all components of the NCFMAS system rather than considering mantle composition as an equilibrium assemblage of basalt and harzburgite as in our previous study [*Khan et al.*, 2009]. The immediate benefit of this approach is the greater leniency in modeling mantle chemistry, albeit at the expense of decreasing model parameter resolution. In summary, there is no unique way of parameterizing the system under study; thus, the results presented here reflect the particular, near-minimal, parameterization chosen. Also, as we disregard uncertainties related to mineral physics para-

eters and the thermodynamic formulation, derived uncertainty estimates on sampled thermochemical parameters appear to be better constrained than they are in reality. Finally, our tectonics-based regionalization scheme employed here adequately describes upper mantle lateral structure, but it is less appropriate in the lower mantle. As a result of these limitations, most notably the latter, any inferences drawn from the results that follow are first order. However, as shown and discussed in the following, our results are supported by many previous studies of lithospheric and upper mantle thermal and compositional structure and the predictions of large-scale tomographic  $P$  and  $S$  wave velocity models.

## 5. Results and Discussion

### 5.1. Calculated Data

[41] A typical fit to data is shown in Figure 3 for tectonic regions in Antarctica (Q) and North America (p). All Love and Rayleigh wave branches are seen to fit data within estimated uncertainties.

### 5.2. Isotropic Physical Properties

[42] Isotropic physical properties are shown in Figures 4 ( $V_s$ ), 5 ( $V_p$ ), and 6 ( $\rho$ ) at various depths in the form of the most probable model, upper, and lower 75% credible intervals. For comparison, we have also included a number of seismic tomography models: vox5p07, SAW642AN, S362ANI, and SPRD6. For comparison with our results, we only show the average values of all these models within the 27 tectonic regions of Figure 1. The  $P$  wave velocity model vox5p07 was obtained by *Boschi et al.* [2008] using the method of *Boschi and Dziewonski* [1999] and inverting *Antolik et al.*'s [2001] improved database of  $P$ ,  $PKP$ , and  $PcP$  traveltime observations from the International Seismological Centre bulletins. The model vox5p07 is parameterized in terms of 15 layers of equal-area ( $5^\circ \times 5^\circ$  at the equator) pixels. Models SAW642AN and S362ANI are recent 3-D anisotropic shear wave velocity models of the Earth's mantle and were derived by *Panning and Romanowicz* [2006] and *Kustowski et al.* [2008], respectively. Model S362ANI was obtained using large data sets of surface wave phase anomalies, body wave travel times, and long-period waveforms, whereas SAW642AN relied entirely on the use of surface wave and body waveform data. Finally, for comparison with density, we use model SPRD6, which constrains only the very long wavelength density structure of the Earth's mantle and is based on a large collection of normal mode data and free-air gravity constraints [*Ishii and Tromp*, 2001, 2004]. Although controversial (see, e.g., the works of *Resovsky and Ritzwoller* [1999], *Kuo and Romanowicz* [2000], and *Romanowicz* [2001] for discussions), we include the model here as it is the only tomography model that so far has provided independent information on the global density structure of Earth's mantle.

**Table 2.** A Priori Bounds on Anisotropy Parameters

Depth (km)	$\xi$	$\phi$	$\eta$
0–25	1	1	1
<300	0.99–1.15	0.9–1.15	0.9–1.15
>300	0.97–1.05	0.97–1.05	0.97–1.05

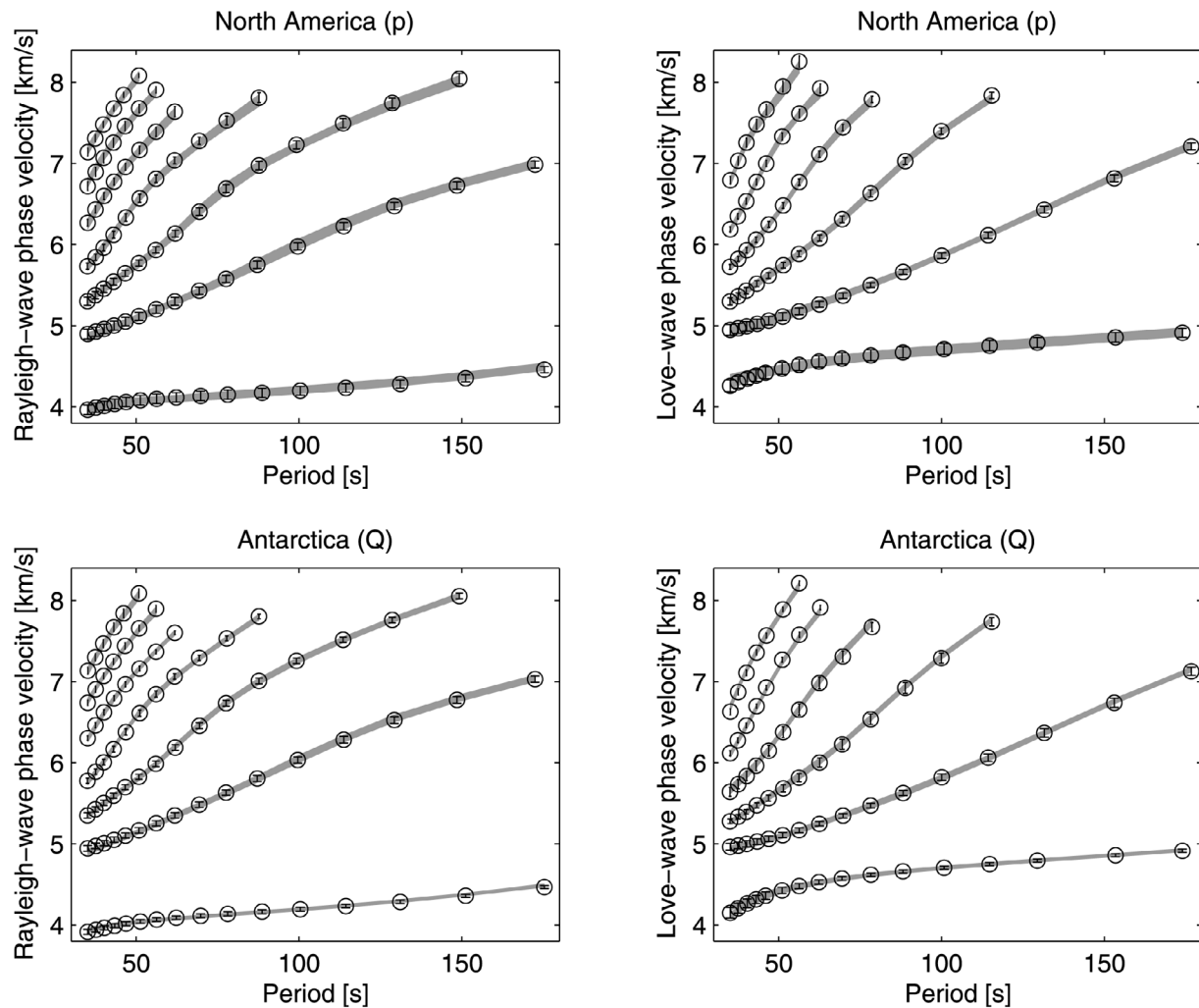


**Figure 3.** Comparison of calculated (shaded lines) and observed Rayleigh and Love wave phase velocities (circles), including uncertainties (error bars), for two different tectonic settings.

[43] Seismic tomography models are essentially derived as perturbations with respect to a spherically symmetric reference model. Such models, however, have little meaning in the present context, rendering comparison with the latter models difficult. To circumvent any such problems, we display absolute values rather than perturbations from some reference model in line with arguments put forward by Kennett [2006].

### 5.2.1. Mantle $S$ Wave Velocity Structure

[44] The major feature of our  $S$  wave velocity maps perceptible at 100 km depth is the ocean-continent delineation. We find the oceans to be slower than continents, with oceanic lithosphere becoming faster at increasing distance from the ridges. The same features recur in SAW642AN and S362ANI as well as in many other fundamental mode

seismic surface wave tomography studies [e.g., *Trampert and Woodhouse, 2001; Ekström et al., 1997; Shapiro and Ritzwoller, 2002; Boschi and Ekström, 2002; Lebedev and van der Hilst, 2008*]. The ocean-continent contrast seems to continue into the upper mantle and is palpable down to a depth of 250 km, in line with both S362ANI and SAW642AN and the recent study by *Lebedev and van der Hilst [2008]*, as well as model S20RTS of *Ritsema et al. [2004]*.

[45] These remarks are confirmed by Figure 7, which shows sampled marginal posterior pdfs (henceforth simply pdfs) for a set of selected regions representative of oceanic (oc), cratonic (cr), and continental (co) provinces. The pdfs for shear wave velocities at 100 and 250 km depths (Figures 7a, 7b, 7g, 7h, 7m, and 7n) seemingly imply that  $V_s^{\text{oc}} < V_s^{\text{co}} < V_s^{\text{cr}}$ . This is also the case for the age-dependent

**Figure 4.** Tectonically regionalized global isotropic shear wave velocities at several depths in the upper mantle, transition zone, and upper part of the lower mantle obtained here and in two previous seismic tomography shear wave velocity models (d) SAW642AN and (e) S362ANI. Figures 4a, 4b, and 4c are lower 75% credible interval, most probable model, and upper 75% credible interval, respectively. Lower and upper credible intervals are measures of uncertainty (see text for further elaboration).

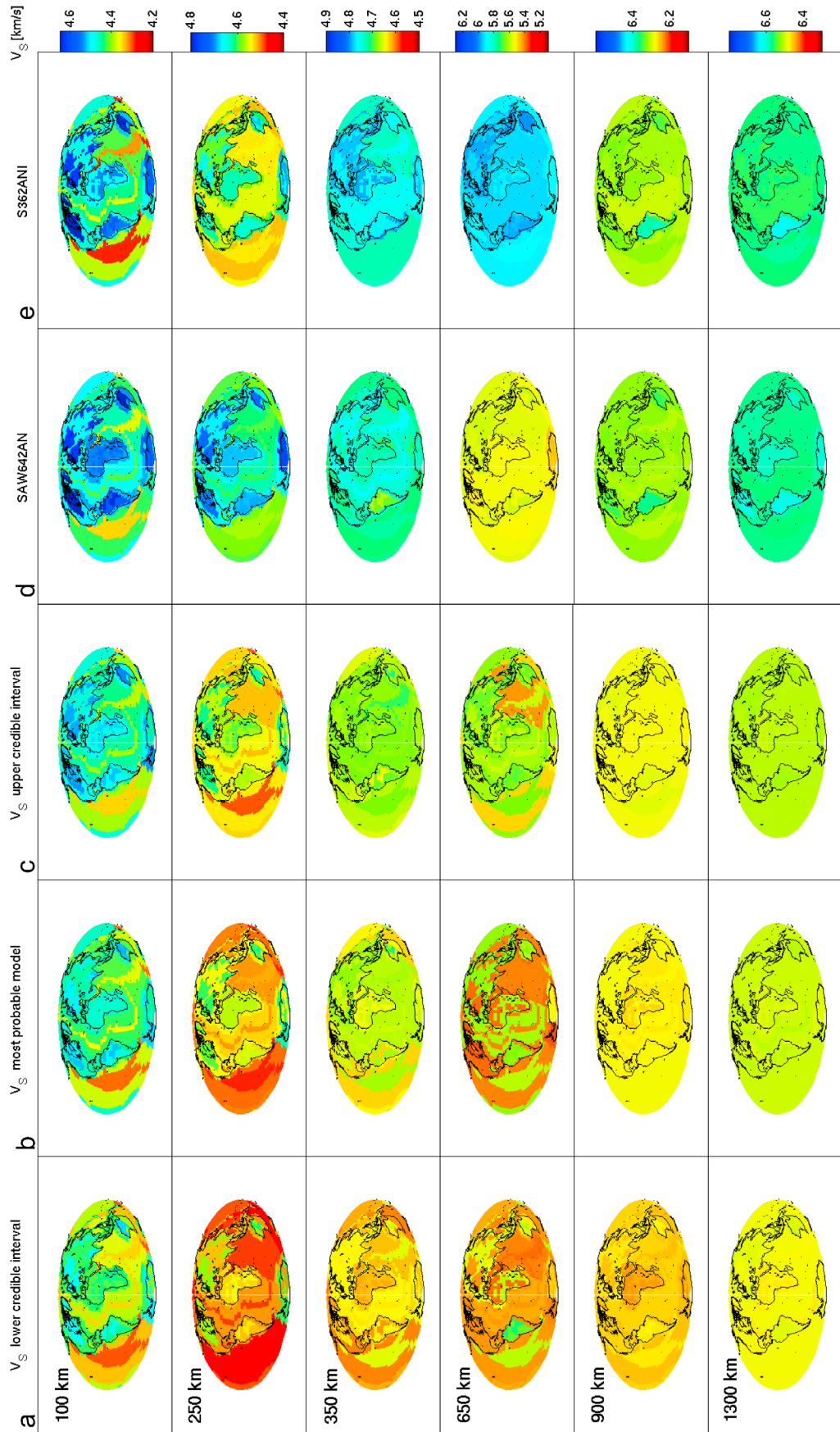
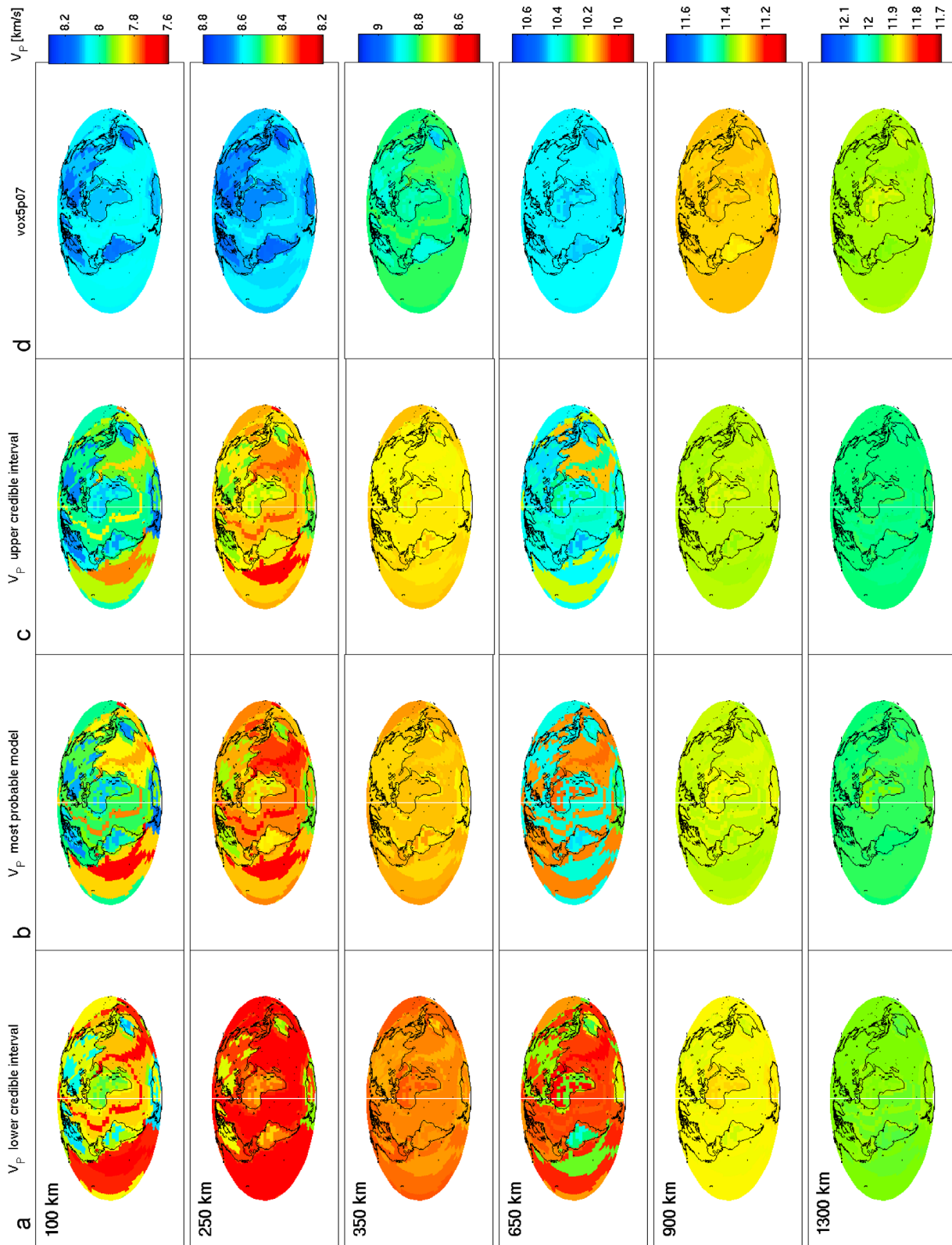
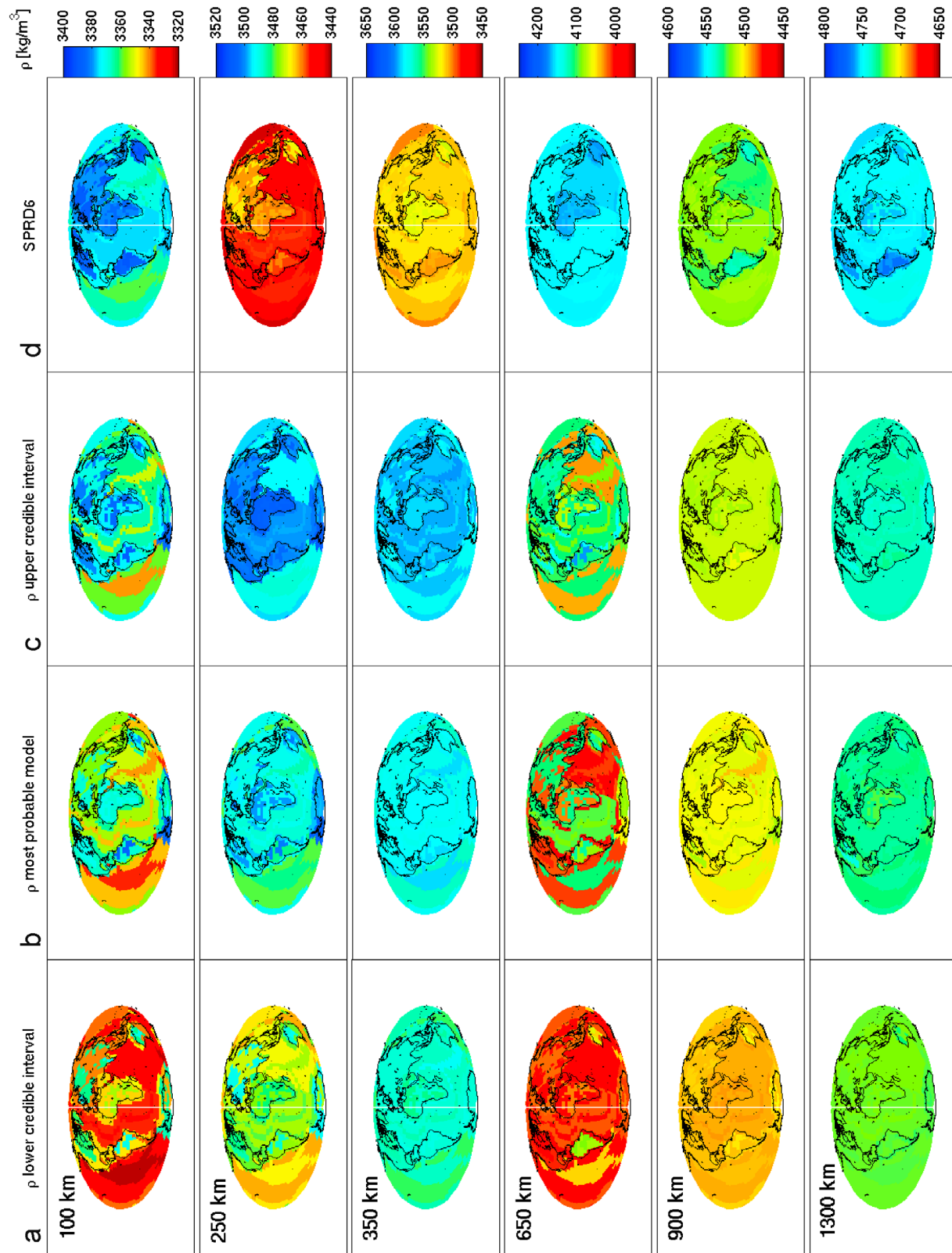


Figure 4



**Figure 5.** Tectonically regionalized global isotropic  $P$  wave velocities at the same depths as in Figure 4. (a) Lower 75% credible interval, (b) most probable model, and (c) upper 75% credible interval. (d) The seismic tomography  $P$  wave velocity model vox5p07.



**Figure 6.** Tectonically regionalized global densities at the same depths as in Figures 4 and 5. (a) Lower 75% credible interval, (b) most probable model, and (c) upper 75% credible interval. (d) Seismic tomography density model SPRD6.

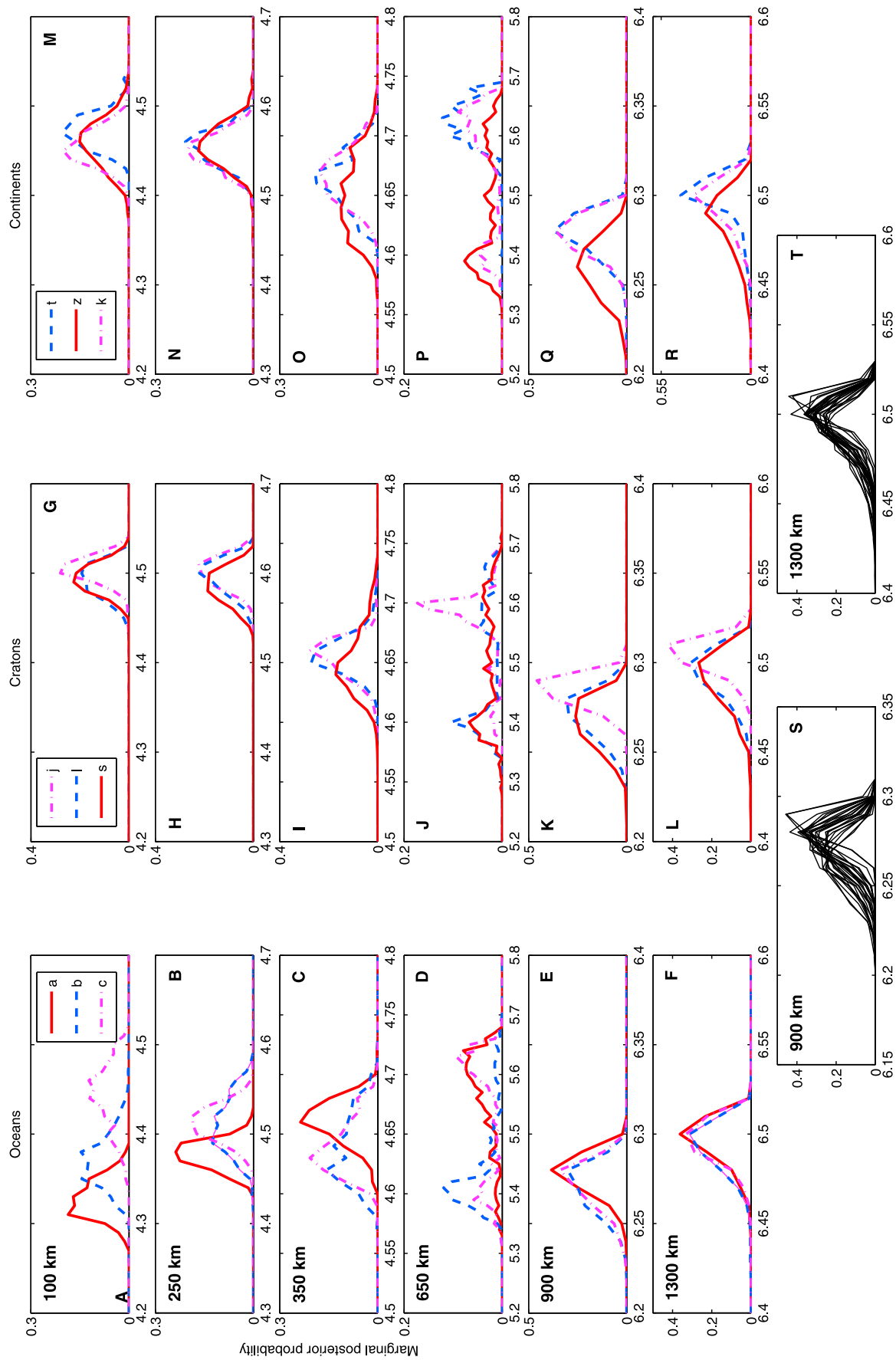


Figure 7

oceanic lithosphere signal at 100 km depth (Figure 7a), where  $V_s^a < V_s^b < V_s^c$ , with a, b, and c denoting young, intermediate age, and old oceanic lithosphere, respectively. At 350 km depth, the pdfs generally start to overlap across the various regions, with most of the probability mass confined to the range 4.6–4.7 km/s for all three tectonic provinces shown in Figures 7c, 7i, and 7g. This is a partly expected result given our regionalized parameterization, designed to describe relatively shallow, tectonics-related structure; but it is also in agreement with the idea that heterogeneity decreases with increasing upper mantle depth. Extending the analysis of Figure 7 to all 27 provinces (not shown for brevity) confirms that the signature of oceans, continents, and cratons is discernable in  $V_s$  at 250 km depth, less so at 280 km, and disappears at 310 km.

[46] With regard to the depth extent of continental roots, most of the major cratons seen here, including the Canadian (CS), Baltic shield and East European platform (BS), Siberian platform (SIB), Indian shield (IND), and Western Australia (AUS) are apparent as regions of high velocity down to 200–250 km depth. They appear to vary regionally and are thus consistent with smaller-scale variations suggested by tomographic and regional-scale studies [e.g., Zielhuis and Nolet, 1994; Ekström and Dziewonski, 1998; Simons et al., 1999; Debayle and Kennett, 2000; Yoshizawa and Kennett, 2004; Sebai et al., 2006; Marone et al., 2006; Lebedev et al., 2006, 2009], as well as from studies combining gravity with seismic tomography models [e.g., Forte et al., 1994; Deschamps et al., 2001].

[47] In the TZ our maps generally appear to show more structure than is present in either SAW642AN and S362ANI. This, however, is the product of a generally less well determined TZ as evidenced in Figures 7d, 7j, and 7p. The sampled pdfs for  $V_s$  in the TZ are broad, and while peaks do appear, they are less robust (for further discussion, see section 5.3). In the upper part of the lower mantle (henceforth simply the lower mantle), our maps, SAW642AN, and S362ANI seem to become relatively smooth and remain so down to 1300 km depth, defining the extent to which we can presently sense. The pdfs in Figures 7e, 7f, 7k, 7l, 7q, and 7r, and in particular in Figures 7s and 7t, where all sampled regional  $V_s$  pdfs at 900 and 1300 km depth have been compiled, support this contention. This observation suggests that heterogeneities at large depth are small and possibly insignificant compared to those at shallower depth, or, in other words, for increasing lower mantle depths the shear wave velocity structure becomes homogeneous and converges on a 1-D-like model, much as the seismic tomography models converge on a particular spherically symmetric reference model. The absence of strong heterogeneities at long wavelengths below 650 km is observed in both S362ANI and SAW642AN as well as in most previous  $S$  wave tomography studies as a transition to spectrally whiter low-amplitude midmantle isotropic velocity anomalies.

[48] Disregarding amplitudes when comparing our results with SAW642AN and S362ANI, we observe that all three

models seem to overlap to a large extent in the upper mantle, in agreement with correlations performed by *Kustowski et al.* [2008]. These authors found high correlations between S362ANI, SAW642AN, and S20RTS down to 250 km depth. Depending on the model (SAW642AN or S20RTS), correlation was generally low between the TZ and 1700–2000 km depth. The discrepancy between SAW642AN and S362ANI is also seen in the maps shown here for depths  $>350$  km. As a more direct method of comparison, we have plotted in Figure 8 the 1-D profiles of  $S$  wave velocity (as 95% credible intervals) for the tectonic regions investigated in Figure 7. We also include PREM and 1-D models extracted from S362ANI for the same tectonic locales. Apart from differences in amplitude, which is a well-known problem of tomographic models, and the absence of detailed structure in S362ANI related to mineral phase transformations and changes in mineralogy in general, our radial profiles overall display the same pattern of velocity variations with regard to PREM as S362ANI. For a more detailed discussion of these differences, we refer the reader to section 5.4 of our previous study [*Khan et al.*, 2009].

[49] In the following, we abstain from showing mantle attenuation structure simply because it is not so well resolved with the data considered here. This stems from the large uncertainties on the parameters (see equation (1)) that go into computing  $Q$ . However, to ascertain that our results were not influenced to any large extent by a particular choice of parameters ( $Q_0$ ,  $\alpha$ ,  $E_a$ , and  $V_a$ ) and thus  $Q$ , we undertook several inversions with different sets of parameter values (10%–20% variation) and verified that this incurred little change to our results.

### 5.2.2. Mantle $P$ Wave Velocity Structure

[50]  $P$  wave velocity maps are shown in Figure 5 and display the same quantitative ocean-continent differences discussed earlier for our  $S$  wave velocity model, in particular at a 100 km depth, where mantle regions beneath mid-ocean ridges are marked by low  $P$  wave velocities and stable continents are associated with high velocities. These regions are much less conspicuous in the seismic tomography model vox5p07 at the same depth with a peak-to-peak velocity difference of 0.15 km/s in comparison to  $\sim 0.5$  km/s here. The ocean-continent difference is barely visible in our maps at 250 km depth, while at 350 km depth  $P$  wave velocities are very uniform. In the TZ, as in the case of  $S$  wave velocities,  $P$  wave velocity structure is less well constrained. In the lower mantle (900–1300 km depth) our velocity maps again become relatively uniform. In comparison, vox5p07 is noticeably uniform over most of the depth range just discussed. In the upper mantle vox5p07, like SAW642AN, is shifted toward higher velocities, with some overlap at 650 km depth, while in the lower mantle vox5p07 is very slightly “red-shifted” relative to our maps.

### 5.2.3. Mantle Density Structure

[51] Maps of mantle density structure are shown in Figure 6 and, as in the case of both our  $P$  and  $S$  wave velocity maps, ocean-continent density differences are distinguishable at

**Figure 7.** Marginal posterior probability density functions showing sampled  $S$  wave velocities at various depths in the upper mantle, transition zone (TZ), and lower mantle for a number of different tectonic regions: (a–f) Pacific, (g–l) cratonic, and (m–r) continental, as well as all tectonic provinces at (s) 900 km and (t) 1300 km depth. Letters in the legends refer to Figure 1.

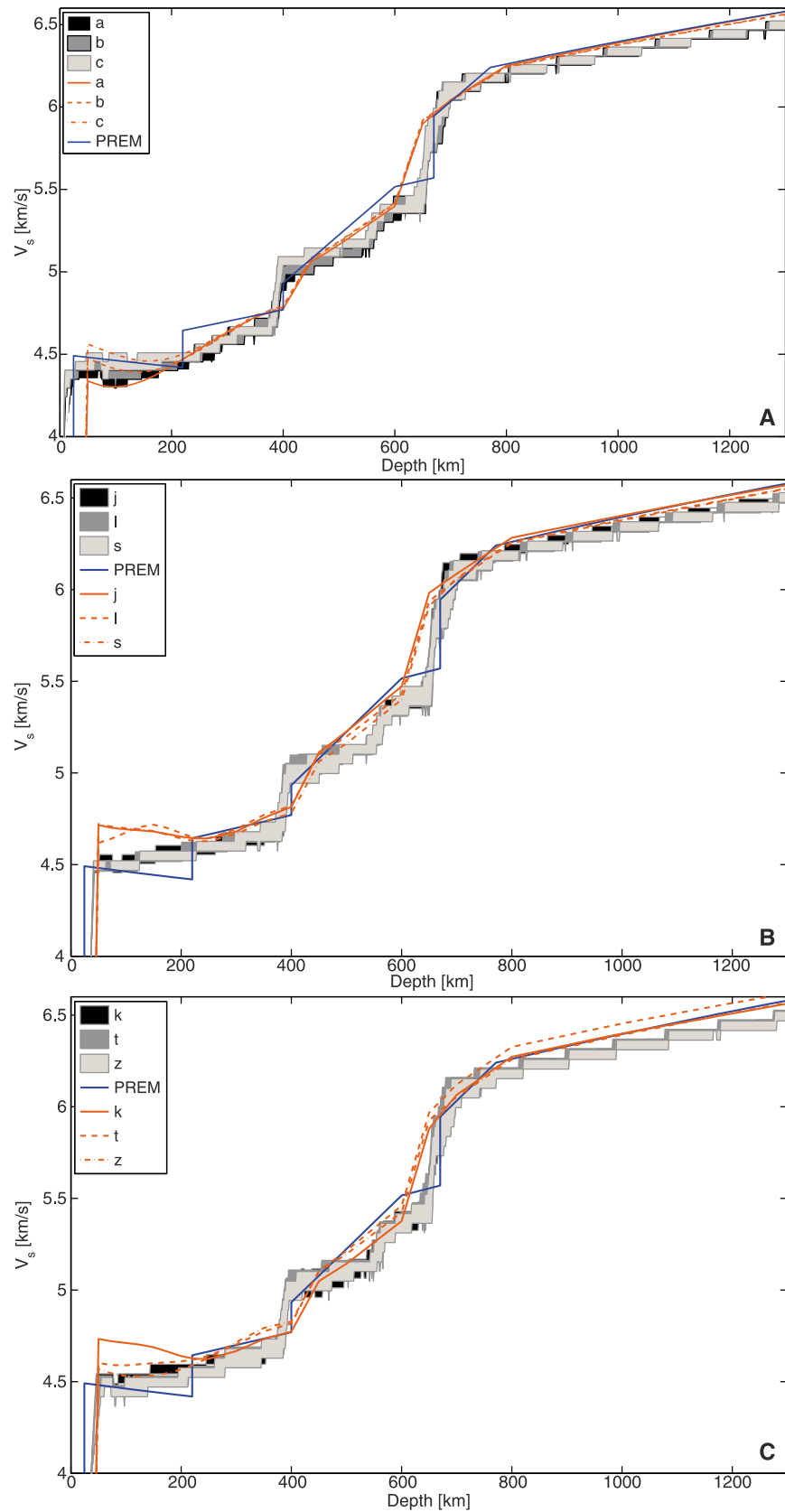


**Figure 8.** Radial profiles of shear wave velocity from the surface and down to a depth of 1300 km beneath different tectonic regions: (a) Pacific Ocean, (b) cratons, and (c) continents. Profiles derived in this study are shown as 95% credible intervals, whereas preliminary reference Earth models and 1-D models extracted from S362ANI are shown as blue and red lines, respectively.

100 km depth. Oceanic lithosphere appears less dense than stable continental lithosphere, while most cratons seem to be denser than surrounding continental lithosphere. These regional variations have more or less disappeared at 250 km depth, in line with the hypothesis of *Jordan* [1978] as to the stability of cratons (see also section 5.5). As in the case of both *P* and *S* wave velocity models, TZ density structure is not well determined, whereas in the lower mantle (900–1300 km depth) the density maps are seemingly uniform. Although seismic tomography model SPRD6 is shown for comparison, this particular model is not easily compared with our models here, because of its low-degree nature. Model SPRD6 consists only of even degrees 2, 4, and 6, which explains why near-surface features are less pronounced. Also, amplitudes of density anomalies in model SPRD6 are generally small, rendering the distinction between oceans and continents in the upper mantle much less conspicuous, in particular at 100 and 250 km depth.

### 5.3. Mantle Composition

[52] Mantle compositions are summarized in Figures 9 and 10 in terms of magnesium number (Mg #) (molar Mg/[Mg+Fe]) and Mg/Si ratio (in weight percent), since variations in the major elements FeO, MgO, and SiO<sub>2</sub> most significantly affect elastic properties as shown in an earlier study of ours [*Khan et al.*, 2008].

[53] From the compositional maps the ocean-continent signature is discernable at a depth of 100 km, which, within the uncertainties of the maps, point to FeO enrichment of the oceans relative to the continents, with differences ranging from 0.5 to 1 wt %. Although an age-dependent signature also seems to be extant, indicating that younger oceanic lithosphere is relatively more enriched than older oceanic lithosphere, we do not consider this to be a robust result (see also Figure 11). The continental FeO depletion is particularly noticeable for the cratons. FeO contents at 100 km depth for the cratonic regions of North America, the Baltic shield and East European platform, the Siberian platform, the Indian shield, and Western Australia are observed to be between 7.3 and 8.0 wt % (Mg # ~0.895–0.91), in comparison to 7.8–8.8 wt % (Mg # ~0.875–0.9) for the oceanic lithosphere. The cratons of South America, West Africa, and South Africa are less prominent.

[54] Considering variations in MgO and SiO<sub>2</sub> (Mg/Si), we generally find that while the ocean-continent delineation is more difficult to observe, cratons are to some extent distinguishable from the surrounding continental and oceanic lithosphere due to their higher MgO (38–40 wt %) and lower SiO<sub>2</sub> content (43–46 wt %), corresponding to a Mg/Si ratio in the range 1.2–1.4. In comparison, oceanic lithosphere ranges from 1.05 to 1.25.

[55] To ascertain the robustness of these results, we investigated the posterior pdfs for individual regions. The results are summarized in Figure 11, which shows posterior pdfs for a number of cratonic (NA, IND, AUS, BS, and SIB) and oceanic (Pacific) regions. Comparing the pdfs for cratons (Figures 11b, 11d, and 11f) with those for the Pacific ocean (Figures 11a, 11c, and 11e) appears to show that cratons are depleted in FeO and have higher Mg # as well as Mg/Si ratio relative to oceanic regions. We also investigated the pdfs for the other regions (not shown) and found the same pattern for the Atlantic and Indian oceans as for the

Pacific (i.e., low Mg # and Mg/Si ratio), while the pdfs for other continental regions were less conspicuous. Although it is apparent from Figure 11 that composition is less well resolved (compare prior and posterior), it is nonetheless the case that the compositional trends between cratonic and oceanic lithosphere observed here are relatively robust.

[56] These results, in particular those for the cratons, generally persist with relatively minor changes to a depth of 250–300 km, beyond which the cratonic signal disappears. This indicates that ocean-continent differences appear to extend to at least 200–250 km depth, whereas the cratonic roots, signified by FeO depletion and thus high Mg #, possibly extend a little deeper.

[57] Although it is beyond the scope of the present study to discuss all the evidence in support of compositional differences within the continental lithosphere, it should be noted that all cratons show strong positive velocity anomalies that are believed to be nonthermal in origin and attributed to chemical depletion of the mantle (mainly Fe and Al during melt extraction), in agreement with xenolith data (for details we refer to reader to the review by *Artemieva* [2009]). *Gaul et al.* [2000], for example, found a general decrease in Mg # for Precambrian lithospheric mantle with age. Mg # decreases from 0.92–0.94 for Archean lithospheric mantle to 0.915–0.925 and down to 0.90 for Proterozoic and Phanerozoic continental lithospheric mantle, respectively. In spite of the low vertical resolution of our model, the same trend is observed here for the Australian and North American continents. In addition, a suite of analyses including experimental studies of cratonic peridotites, mantle xenoliths, heat flow analyses, and seismologically related mantle flow studies add further support to the contention of a compositionally distinct continental lithosphere [e.g., *Boyd*, 1989; *Rudnick et al.*, 1998; *Griffin et al.*, 1999; *Jaupart and Mareschal*, 1999; *Forte and Perry*, 2000; *Röhm et al.*, 2000; *Deschamps et al.*, 2001; *Kuskov et al.*, 2006; *Artemieva*, 2009; *Afonso et al.*, 2010].

[58] Keeping in mind that our tectonic parameterization becomes less well suited for modeling and interpreting variations in the TZ and lower mantle, the compositional signal in the TZ is seen to be more complex with little or no correlation with surface tectonic features, as expected. Moreover, TZ compositional structure is generally not well resolved, which explains the broad nature of the marginal pdfs for *V<sub>S</sub>* shown in Figures 7d, 7j, and 7p. In the lower mantle the compositional maps are remarkably uniform and any compositional variations have seemingly been smoothed out.

[59] Although the lower mantle appears to be relatively uniform in composition, the compositional maps presented here point to first-order compositionally distinct upper and lower mantles, with the TZ possibly acting as a compositional boundary over which the change from generally lower Mg # and higher Mg/Si ratios to the reverse (i.e., higher Mg # and lower Mg/Si ratios, respectively) takes place. Further perusal of maps of SiO<sub>2</sub> and FeO content as well as individual pdfs of SiO<sub>2</sub> and FeO for various regions in the lower mantle indeed reveals SiO<sub>2</sub> and FeO contents in excess of 48.5 wt % and less than 6.5 wt %, respectively. This is generally somewhat higher and lower, respectively, than various literature estimates of the bulk silicate composition of the Earth's mantle, where SiO<sub>2</sub>/FeO values typically around (45–46 ± 0.5–1.3)/(7.5–8.1 ± 0.1–0.8) wt % are

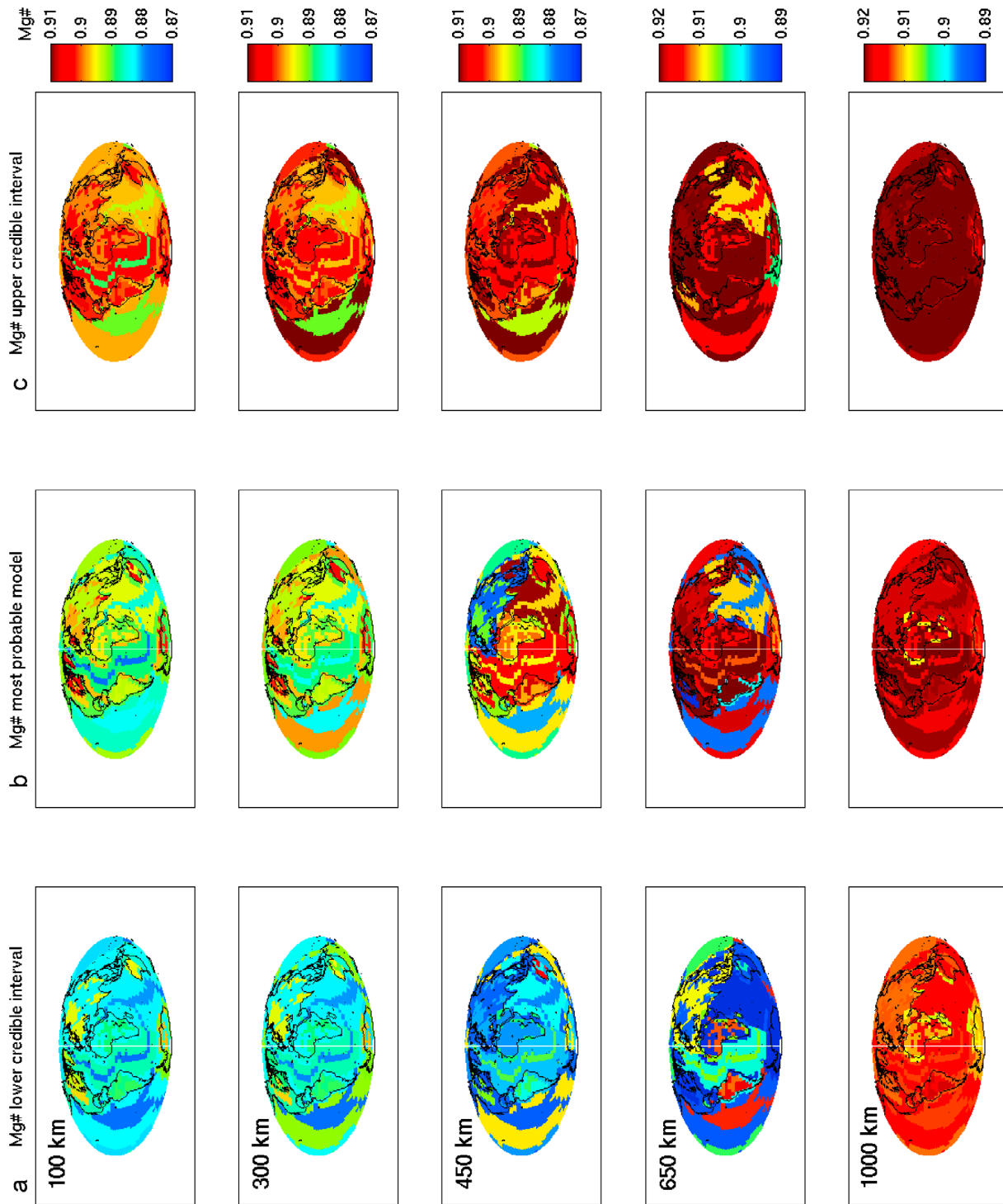


**Figure 9.** Tectonically regionalized compositional maps showing global variation in magnesium number (Mg #) at various depths in the upper mantle, TZ, and lower mantle. (a) Lower 75% credible interval, (b) most probable model, and (c) upper 75% credible interval, respectively.

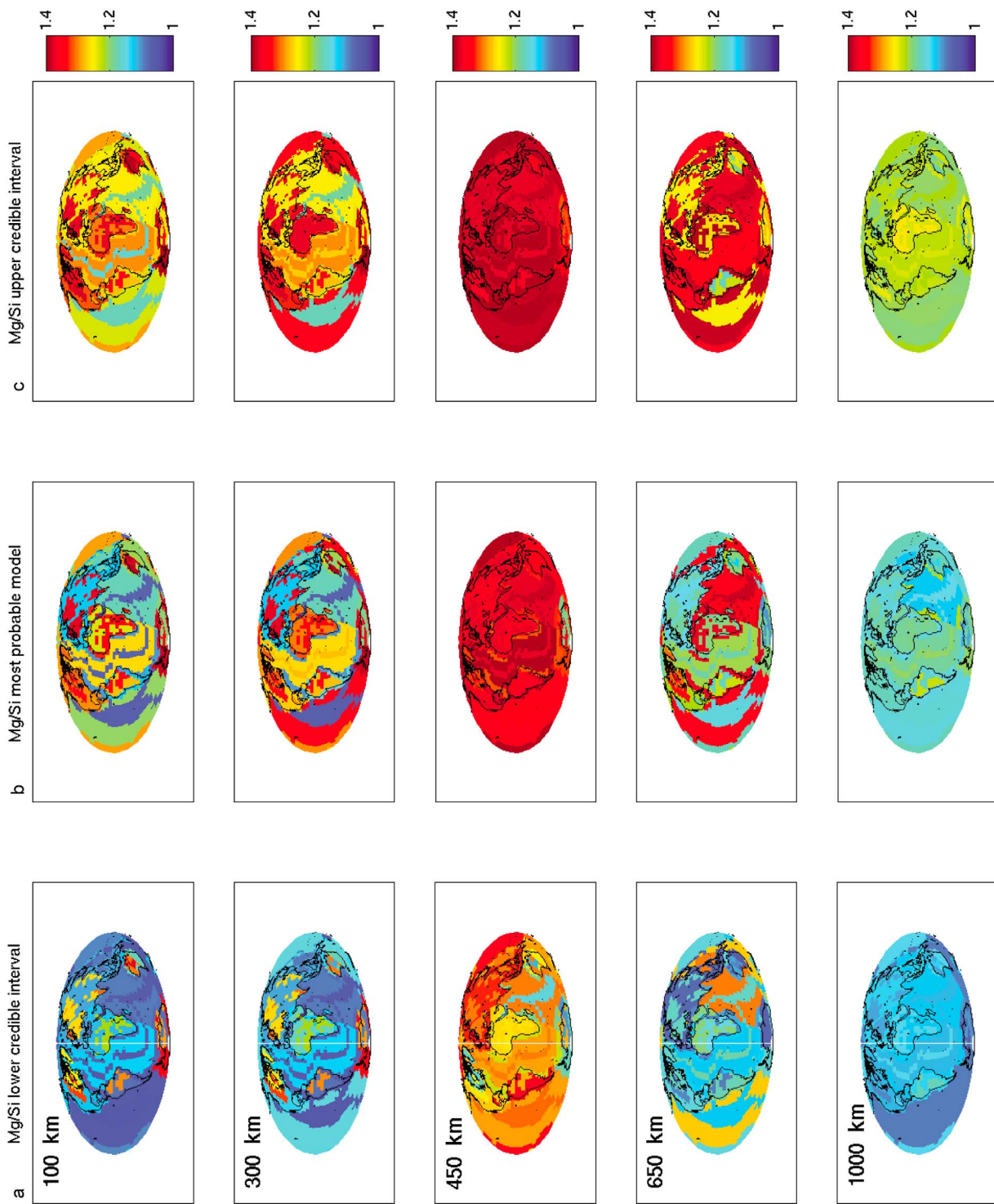


Figure 10. Same as Figure 9 but tectonically regionalized compositional maps showing global variation in Mg/Si ratio at the same depths as in Figure 7.

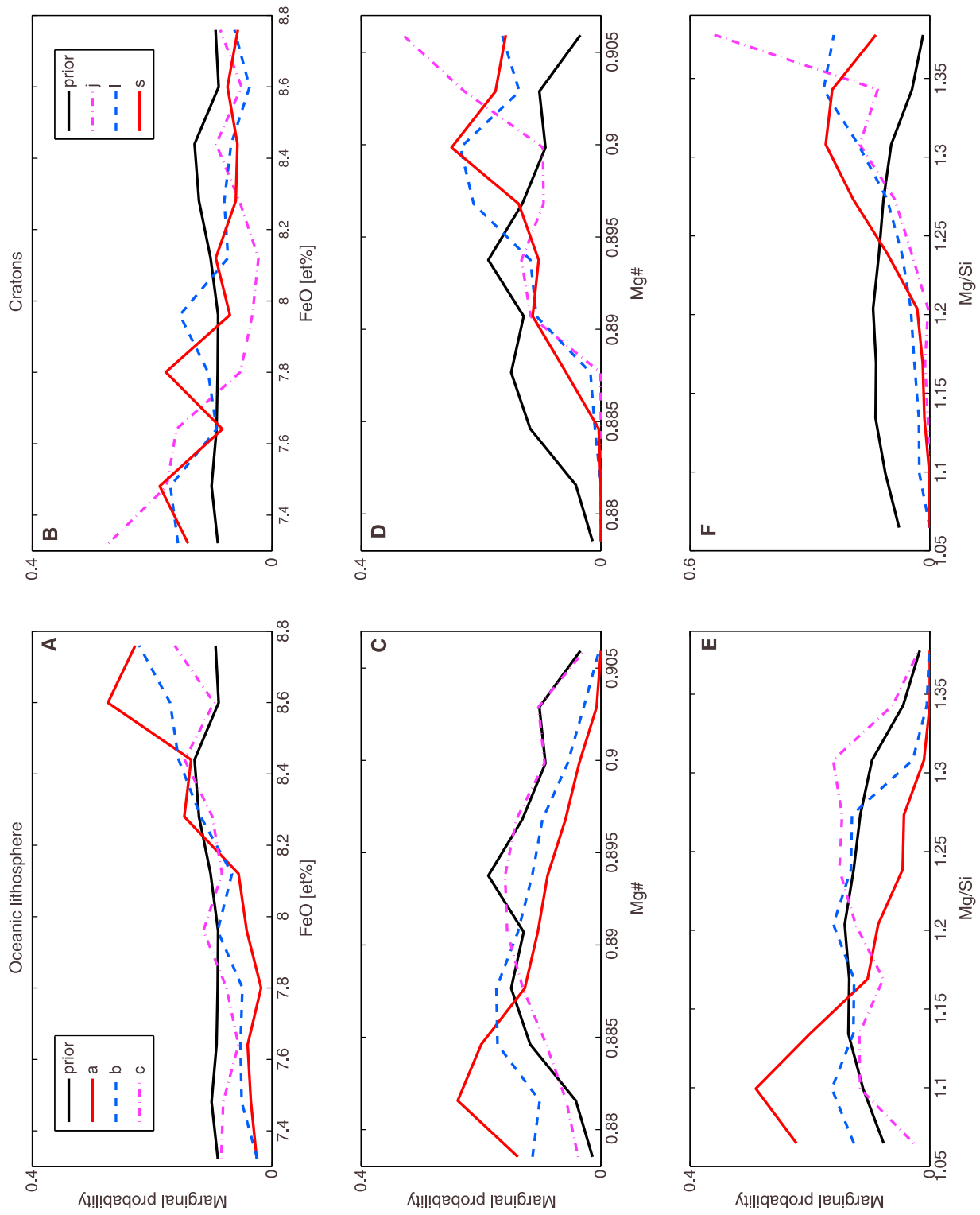


Figure 11

found [e.g., Taylor, 1980; Hart and Zindler, 1986; Palme and O'Neil, 2003; Lyubetskaya and Korenaga, 2007], except for maybe the SiO<sub>2</sub> estimate by McDonough and Sun [1995] of 44.9 ± 4.5 wt %.

#### 5.4. Mantle Temperatures

[60] Thermal maps shown in Figure 12 reveal ocean-continent differences throughout most of the upper mantle in agreement with a number of geophysical studies of the thermal structure of the lithosphere and upper mantle [e.g., Goes and van der Lee, 2002; Röhm et al., 2000; Shapiro and Ritzwoller, 2004; Godey et al., 2004; McKenzie et al., 2005; Faul and Jackson, 2005; Priestley and McKenzie, 2006; Kuskov et al., 2006; Afonso et al., 2008]. In line with these studies, we find that continents appear colder than the surrounding oceans down to a depth of 350 km. In particular, the cratonic regions seem noticeably colder than the surrounding mantle at 250 km and possibly deeper. For the oceans, we find that young oceanic lithosphere throughout our models is relatively hotter than intermediate age lithosphere, which again is hotter than old oceanic lithosphere; that is, we observe that as oceanic plates move away from the ridges they cool as predicted by a simple cooling half-space model as well as recent modeling and heat flow studies [e.g., Stein and Stein, 1992; Ritzwoller et al., 2004; McKenzie et al., 2005]. At a depth of 400 km (not shown), a temperature reversal between oceans and continents apparently occurs such that the previously described ocean-continent thermal variations interchange with continents typically getting hotter than oceanic regions. This is a prominent feature of most seismic models of the upper mantle, where seismic wave velocities under continents change from being faster with respect to oceans.

[61] As a further aid in interpreting the thermal maps, we show marginal pdfs for  $T$  over several selected oceanic, cratonic, and continental regions in Figure 13 in the upper mantle and upper TZ. The ocean-continent contrast is discernable at 100 km depth (compare Figures 13a, 14e, and 14i), as is the age-dependent thermal signature of oceanic lithosphere. In addition, cratonic locales appear slightly cooler than the surrounding continental regions. At 250 km depth the lithosphere beneath oceanic regions has become thermally age-independent (Figure 13b), while differences related to oceans and continents (Figures 13b, 13f, and 13j), as well as intracontinental variations (craton continent), still appear prominent. The ocean-continent contrast seems to persist to 350 km depth, whereas at 450 km depth temperatures across the different regions are likely almost equal (Figures 13d, 13h, and 13l).

[62] Returning to the thermal maps (Figure 12) and relying on analysis of individual pdfs (not shown) appear to suggest, within the uncertainties and the limitations of our model, that no large-scale thermal variations are present in the TZ and lower mantle.

[63] The global thermal maps obtained here for the uppermost mantle are in fairly good agreement with maps produced from global continental heat flow data [Artemieva and Mooney, 2001; Artemieva, 2006]. In particular,

Artemieva [2006] found temperatures around 1000°C–1100°C for the major cratons at 150 km depth. Partial agreement with petrologically inferred mantle temperatures using mantle xenoliths is also found, with our results slightly on the high side compared to the inferred temperatures of 800°C–1100°C at 100 km depth [e.g., Rudnick et al., 1998]. However, any such discrepancies probably result from the large regions that are being averaged in the regionalized approach, in addition to the large uncertainties that typically beset estimates of mantle temperature obtained by petrological means for subcontinental and suboceanic lithosphere (see, e.g., discussion in the work of Artemieva [2009]).

[64] The thermal structure on a more regionalized level was studied by, e.g., Goes et al. [2000, 2005], Goes and van der Lee [2002], and Godey et al. [2004], among others. Temperatures in the upper mantle (200–300 km depth) beneath the North American, European, and Australian continents were inferred by converting regional tomographic velocity models to temperatures using an equation-of-state approach under the assumption that composition is constant (for details regarding methodology the reader is referred to the work of Goes et al. [2000]). The large-scale correlation between temperature and tectonic age observed by Goes and coworkers is also found here, in particular for Australia and North America, where the older parts of the continents are typically observed to be colder than the younger provinces.

[65] The thermal structure of the upper mantle beneath the Pacific was studied by Ritzwoller et al. [2004] using surface wave dispersion measurements and methods along the lines of Goes and coworkers (see Shapiro and Ritzwoller [2004] for details). The authors find average temperatures of 1300°C beneath the ridge at a depth of 100 km, which steadily decreases as the plate moves away from the ridge and cools. For our intermediate age and old Pacific ocean, they obtained temperatures of 1200°C and 1100°C, respectively, which generally accords with what is found here.

[66] The 3-D thermal structure of the TZ was investigated by Cammarano and Romanowicz [2007] and Ritsema et al. [2009] under the assumption that the mantle is adiabatic and made up entirely of pyrolite, thus complicating a direct comparison. The 3-D thermochemical structure of the lower mantle was studied by Trampert et al. [2004], who used constraints from gravity, normal mode splitting functions, and surface wave data to map thermochemical variations in the lower mantle. They found large lateral thermal variations (~400 K) in the depth range 670–1200 km, which far exceeds what we observe in our maps, where variations below the TZ are less than 100°C. In the same depth range, Trampert et al. also found Fe content to vary laterally by up to 2%, in contrast to the picture presented here of a rather uniform lower mantle, compositionally as thermally. However, given our somewhat inappropriate parameterization of the lower mantle, further comparison is not warranted.

#### 5.5. Further Discussion of Thermochemical Structure

[67] From our compositional and thermal maps, variations in Mg # (FeO content) are observed to correlate tightly with

**Figure 11.** Marginal prior and posterior probability density functions depicting sampled variation in FeO content, Mg #, and Mg/Si ratios for various (a, c, and e) oceanic and (b, d, and f) cratonic regions at 100 km depth. Letters in the legends refer to Figure 1.

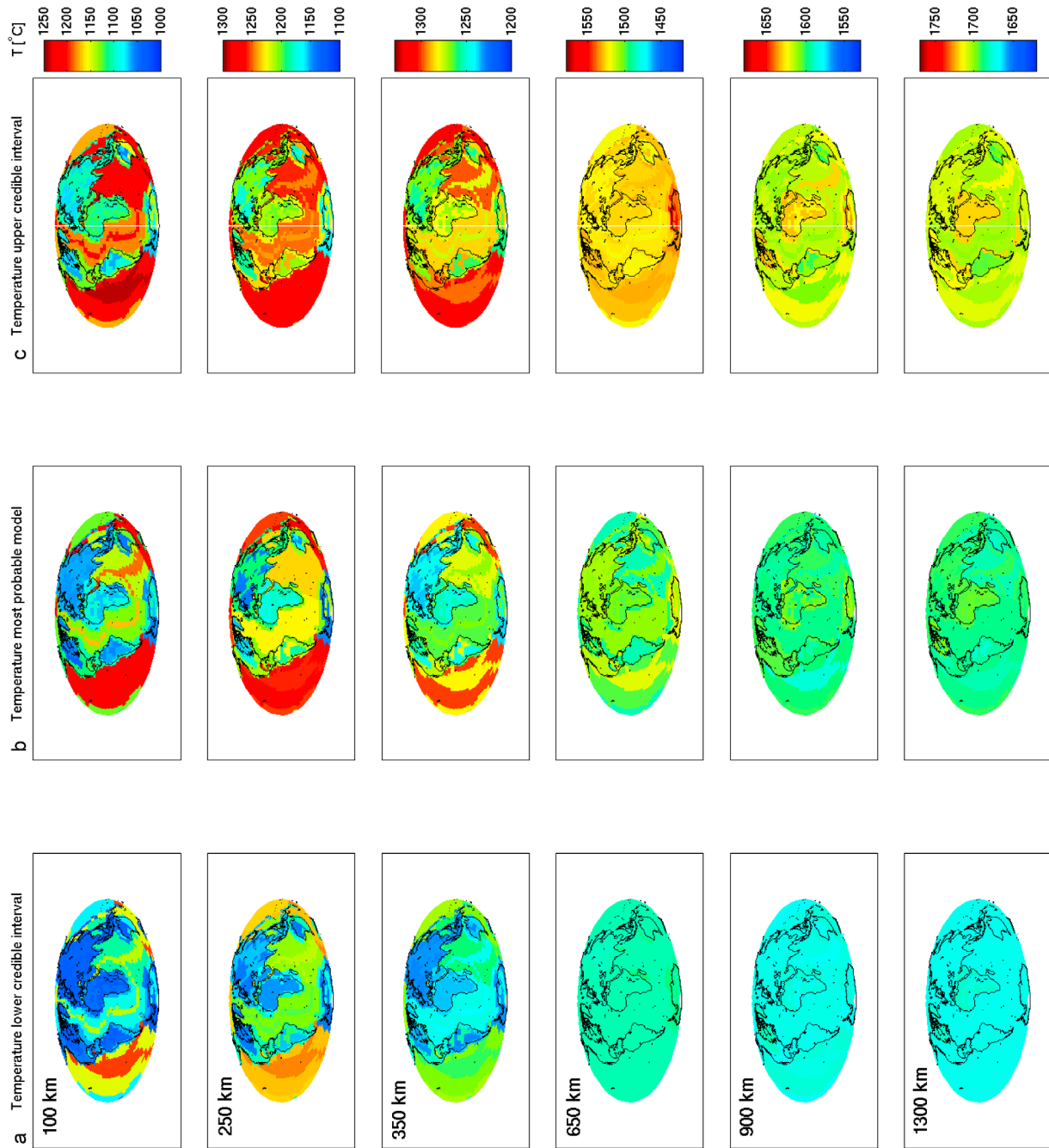
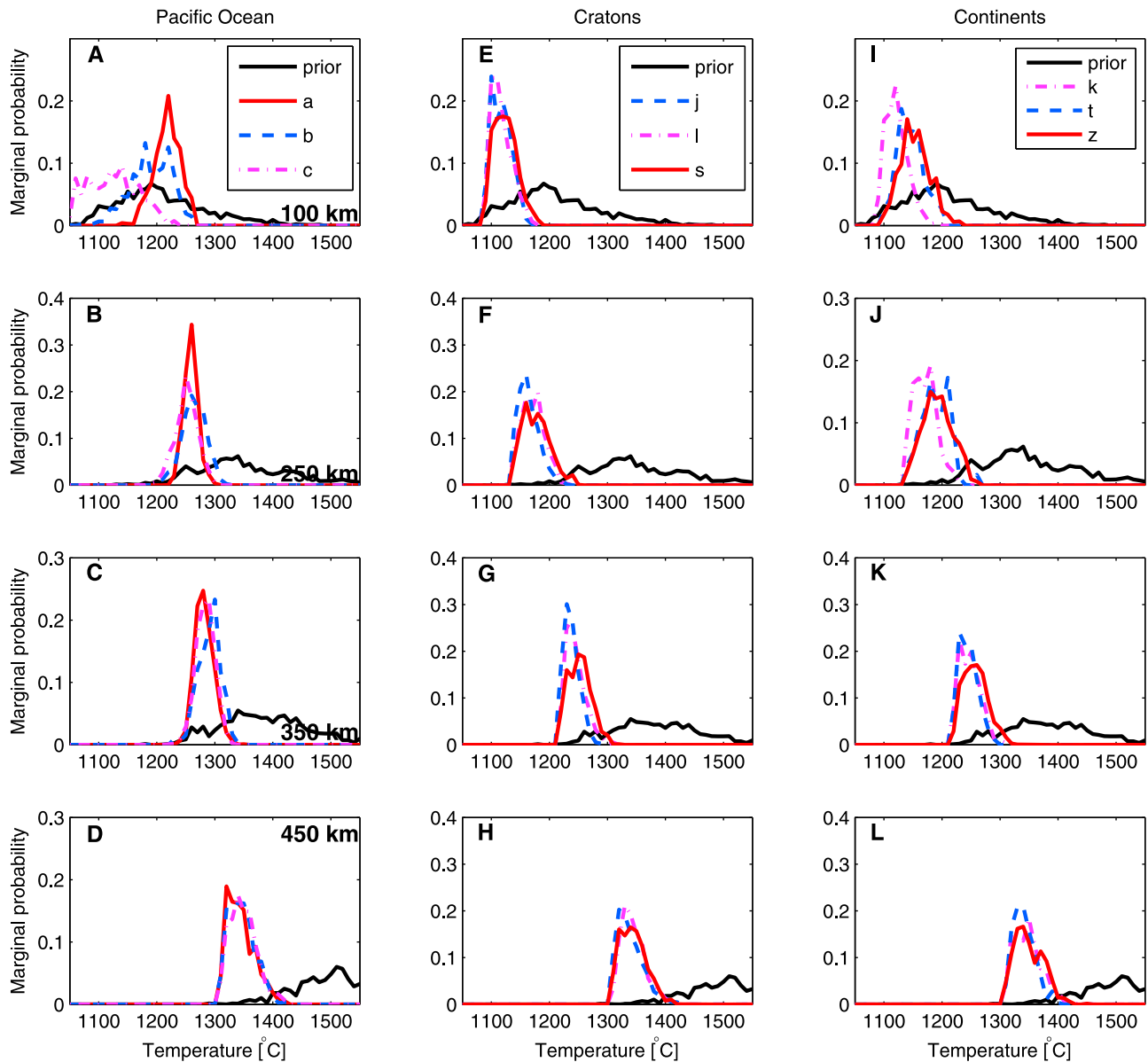


Figure 12



**Figure 13.** Marginal prior and posterior probability density functions showing sampled variation in mantle temperature at various depths in the upper mantle and upper TZ for a number of different tectonic regions: (a–d) Pacific, (e–h) cratonic, and (i–l) continental. Letters in the legends refer to Figure 1.

temperature and tectonic province in the upper mantle. Low Mg # (high FeO content) for cratons, for example, is offset by low temperatures, whereas the opposite is seen to occur over oceanic regions. This had been hypothesized by *Jordan* [1978] as a possible explanation for the stability of cratons using evidence that lithospheric roots beneath Precambrian cratons were observed to be seismically faster than the surrounding mantle.

[68] In interpreting our thermochemical results, it should be kept in mind that these interpretations are based on the

assumption of thermodynamic equilibrium. An alternative, the mechanical mixture model, was found by *Xu et al.* [2008] to provide a better match in the TZ to seismological models such as PREM and AK135 [*Kennett et al.*, 1995] than the equilibrium model. However, these inferences are based on (1) qualitative comparisons and (2) the simplifying assumption of a pyrolytic bulk mantle composition and adiabatic conditions. More succinctly, while the mechanical mixture model plausibly depicts the influence of chemical segregation on the equilibrium model, it cannot be argued to

**Figure 12.** Tectonically regionalized thermal maps showing global variation in temperature at various depths in the upper mantle, TZ, and lower mantle. (a) Lower 75% credible interval, (b) most probable model, and (c) upper 75% credible interval, respectively.



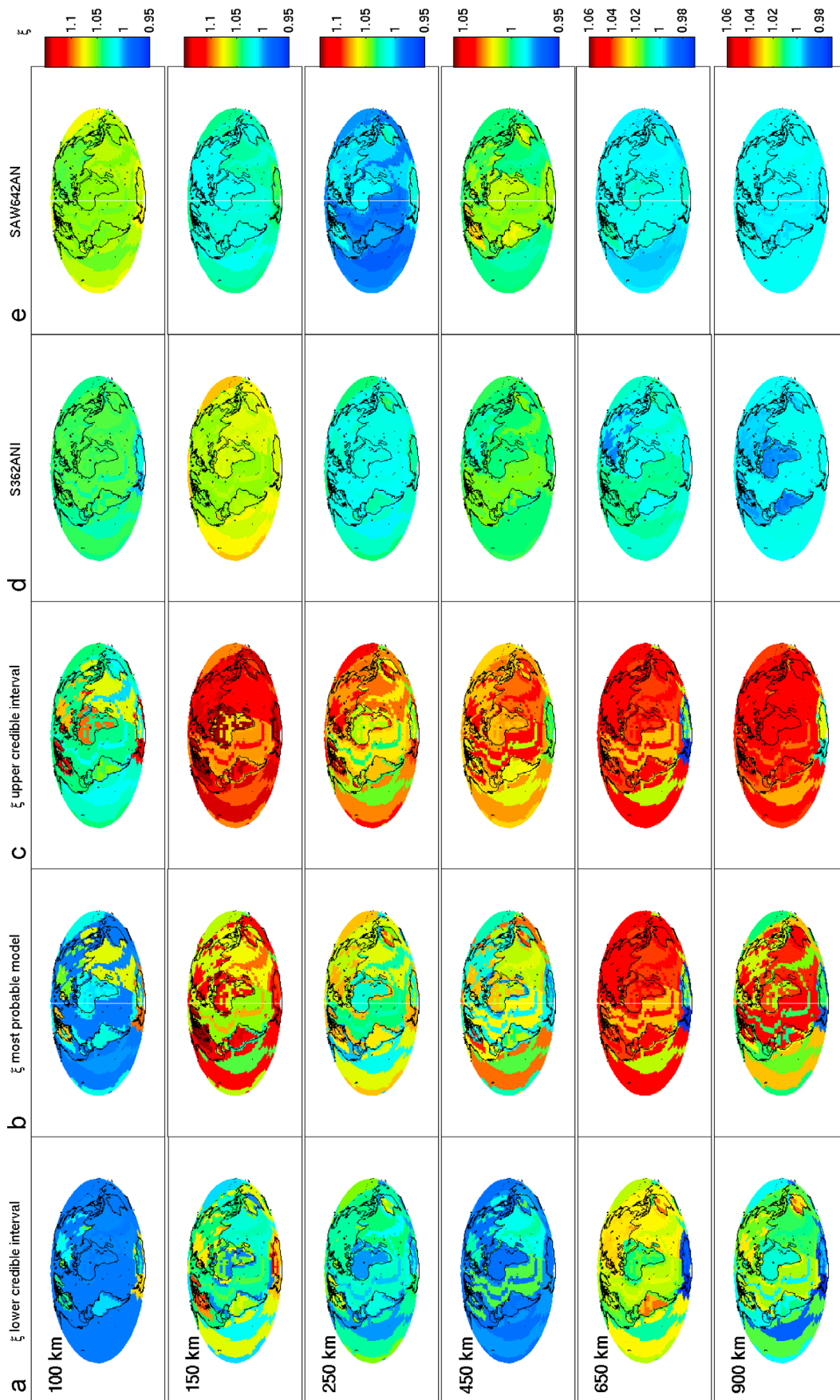


**Figure 15.** (a–c) Same as Figures 4a–4c but for tectonically regionalized anisotropic maps showing global variation in shear wave anisotropy at various depths in the upper mantle, TZ, and lower mantle. Global seismic tomography models (d) S362ANI and (e) SAW642AN, respectively.

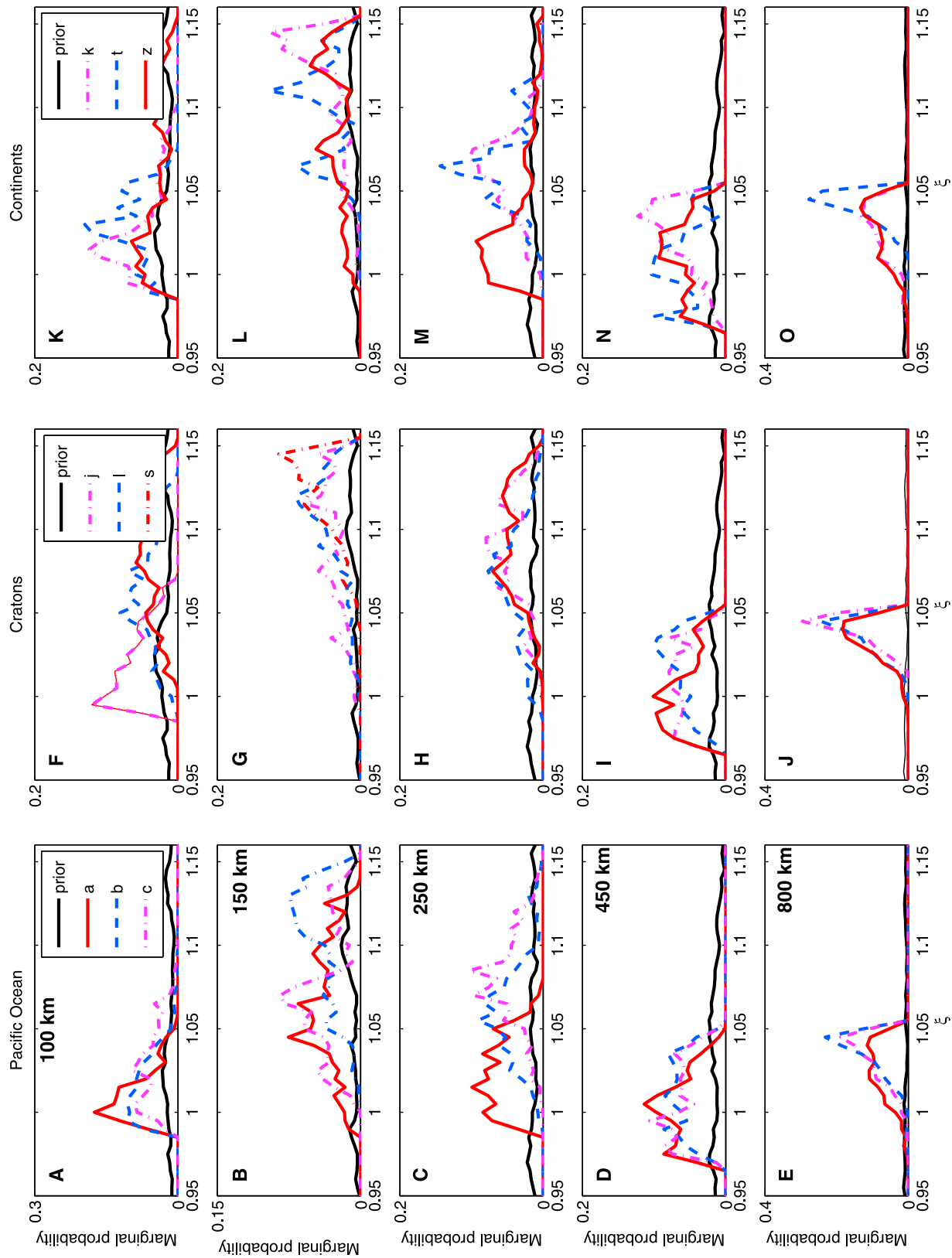


Figure 16

be a more realistic end member for the Earth's mantle because it is inconsistent with mid-ocean ridge volcanism.

[69] The observed thermochemical correlation within tectonic regions seen in our maps is confined solely to the upper mantle. We performed further correlation tests between  $c$  and  $T$  to specifically investigate any trade-off between these parameters. For this purpose we looked at combinations of  $c$  and  $T$  throughout the mantle for all regions studied here. Examples of such correlation tests (here FeO and MgO content versus  $T$ ) in the form of 2-D marginal pdfs for three different tectonic regions at depths of 100, 300, 450, and 1000 km, respectively, are shown in Figure 14. Figure 14 is evidence in support of the overall uncorrelated nature of  $c$  and  $T$ , implying that composition and temperature can be determined independently in agreement with what we found in our previous studies [see, e.g., Khan *et al.*, 2009, Figure 8; Khan *et al.*, 2008, Figure 13]. Figure 14 also shows that while mantle temperatures are reasonably well resolved, composition is less well constrained, in particular in the TZ.

## 5.6. Radial Anisotropic Structure

### 5.6.1. $S$ Wave Anisotropy

[70] Where is the mantle anisotropic? Figures 15 and 16 show global maps of shear wave anisotropy ( $\xi$ ) and marginal pdfs for  $\xi$  at various depths in the upper mantle, TZ, and lower mantle, respectively. Figure 15 includes anisotropic structure from the two recent whole mantle anisotropic tomography models S362ANI and SAW642AN that as in previous plots, have been regionalized. At 100 km depth, oceanic regions generally appear to be less anisotropic than continents, with Figure 16a indicating that a high probability exists for finding  $\xi$  in the range  $0.99 < \xi < 1.02$ , whereas for continents we have  $1.02 < \xi < 1.1$ . At 150 km depth, shear wave anisotropy (henceforth simply anisotropy) achieves its maximum value, which for continents ranges from 1.07 to 1.15 and for oceans from 1.04 to 1.15. At 250 km depth the upper mantle is less anisotropic than at 150 km depth. These results are generally in accord with what has been observed elsewhere at global as well as at regional scales. In particular, the strong positive anisotropic signal beneath the Pacific Ocean first observed by Montagner and Tanimoto [1991], present in both S362ANI and SAW642AN, is also found here. Kustowski [2007, Figure 4.28] and Nettles and Dziewonski [2008], in regionalized tests of their own, observed not only that  $\xi$  anisotropy increased as a function of age for oceanic regions, but that the depth at which the maximum occurred moved deeper. The same observations are made here.

[71] The strong variable anisotropy observed over continental regions is not seen in S362ANI but it figures prominently in the surface wave tomography study of the North American upper mantle of Nettles and Dziewonski [2008]. While there are fewer lateral anisotropy variations in both S362ANI and SAW642AN at a depth of 150 km, these are mostly positive (i.e.,  $\xi > 1$ ) in accordance with what we find

here. The predominantly  $\xi > 1$  anisotropy signal observed beneath continents around 250–300 km depth by Gung *et al.* [2003] figures in SAW642AN as well as our results, but only to a lesser extent in S362ANI. In particular, we find that, beneath continents at a depth of 250 km,  $1.05 < \xi < 1.1$ , whereas underneath oceans,  $1 < \xi < 1.05$ . Both SAW642AN and S362ANI display a distinct  $\xi < 1$  anomaly beneath the East Pacific Rise. This particular anomaly is to some extent also found in our models, where, beneath region c, comprising old Pacific Oceanic lithosphere (not shown), negative shear wave anisotropy is located.

[72] Although a number of studies [e.g., Montagner and Kennett, 1996; Trampert and Van Heijst, 2002; Wookey *et al.*, 2002; Panning and Romanowicz, 2006; Visser *et al.*, 2008b] have pointed to the possible presence of TZ anisotropy, a consensus view about the latter is yet to emerge. In and around the TZ, the global maps and particularly the pdfs shown here provide little substantial evidence for the presence of anisotropy, in agreement with our previous study [Khan *et al.*, 2009]. The pdfs are relatively flat throughout the TZ (Figures 16d, 16i, and 16n), with only very few regions displaying any strong anisotropic signal. This concurs with the conclusions drawn by Kustowski *et al.* [2008] (and on the basis of analysis of the correlation between S362ANI and SAW642AN), who found that anisotropic variations were essentially only consistent in the uppermost (150 km) and lowermost mantle (2800 km). In addition, Kustowski *et al.* [2008] performed a comparison between a whole mantle anisotropic model and a model where anisotropy was confined to depths  $< 400$  km to test consequences on overall data fit. The data fit for the whole mantle model only improved little over their preferred upper mantle-only anisotropic model, suggesting further that data sensitivity to anisotropy in and below the TZ is limited. On the basis of similar tests, i.e., where shear wave anisotropy is limited to the upper mantle, we arrived at results that concur with the latter conclusion of Kustowski *et al.* [2008].

[73] As the discussion so far reflects, most studies have focused exclusively on elucidating  $S$  wave anisotropy, while there has been little discussion of  $P$  wave anisotropy [e.g., Anderson and Dziewonski, 1982; Boschi and Dziewonski, 2000; Beghein and Trampert, 2003]. This imbalance reflects the limited sensitivity of the seismic data to  $P$  wave anisotropy, and it is usual practice in global seismic tomography studies, even in studies considering a multitude of data sets such as those of Panning and Romanowicz [2006] and Kustowski *et al.* [2008], to simply scale  $P$  to  $S$  wave anisotropy using a constant value throughout. Although we inverted for  $\phi$  on a par with  $\xi$ , we abstain from further discussing the results here, given the less well constrained nature of  $\phi$  from long-period surface wave data. We leave it for future studies using appropriate data to resolve  $P$  wave anisotropy.

[74] As concerns  $\eta$ , we find, as in our previous study [Khan *et al.*, 2009] as well as many others, that it is not well constrained by data here. However, we made sure that our

**Figure 16.** Marginal prior and posterior probability density functions showing sampled variation in shear wave anisotropy at various depths in the upper mantle, the upper TZ, and the upper part of the lower mantle for a number of different tectonic regions: (a–e) Pacific, (f–j) cratonic, and (k–o) continental. Letters in the legends refer to Figure 1.

particular parameterization did not lead to perturbation of the radial anisotropic signal found here. We investigated trade-offs between all three anisotropy parameters and found no correlations whatsoever. Similarly, no correlations between anisotropy parameters and any other parameters were observed.

## 6. Conclusion

[75] It has been the purpose here to reconsider the problem of inverting fundamental mode and higher-order Rayleigh (up to sixth order) and Love (up to fifth order) wave phase velocity dispersion curves for Earth's mantle structure (1) using a nonlinear inverse method and (2) to infer global variations in mantle composition and thermal state rather than seismic wave speeds as is typically undertaken in tomography studies. Employing a sampling-based approach to solving the nonlinear inverse problem has the advantage of providing a means to compute robust measures of model parameter uncertainty and resolution, something which has not been fully addressed so far in tomography studies. The purpose of sidestepping seismic wave speeds and instead inverting directly for global mantle composition and temperature stems from the desire to understand the underlying processes that are at the origin of the observed velocity variations which are being imaged at ever-increasing resolution.

[76] Given the choice of composition and temperature as fundamental parameters, and the unifying nature of the thermodynamic method, we obtain a means of constraining shear and compressional wave velocities as well as density without having to impose prior scaling relationships between these parameters. Moreover, given the generality of our formulation, additional independent data sets can easily be incorporated.

[77] To render the use of MCMC methods tractable in the present application, we have had to concede lateral resolution. Our global model has far lower resolution than what is currently attainable in seismic tomography studies and is limited to imaging the very large scales, with compositional and thermal variations varying over the size of continents. Our global parameterization is based on a tectonic regionalization of the Earth as a result of which the model provides a good description of upper mantle variations but is limited to imaging the gross average structure of the lower mantle. However, we would like to reemphasize that at the expense of decreased lateral resolution comes the ability to perform a much improved uncertainty analysis, something which most seismic tomography studies in their present form are lacking.

[78] On the basis of the assumption of a thermodynamically equilibrated mantle, the global maps of mantle composition and temperature imaged here reveal a number of gross features, several of which reinforce results and conclusions from a suite of previous studies, and thus evidence in support of our approach:

[79] 1. The vertical extent of the ocean-continent contrast appears globally to persist to ~250 km depth and varies laterally from 200 to 300 km in depth.

[80] 2. Down to about 200–250 km depth, both cratons and continents appear to be colder than oceans, while cratons are observed to be colder than surrounding continents.

[81] 3. An age-dependent signal is observed for oceanic lithosphere, with young oceanic regions seemingly hotter than their intermediate age and older counterparts.

[82] 4. Highly correlated with these thermal anomalies are compositional variations. The cold continental lithosphere looks depleted in FeO, the equivalent of a high Mg #, relative to oceanic lithosphere. In terms of Mg/Si, cratons can also be distinguished from continents in general and oceans in particular, with a Mg/Si of ~1.2–1.4 and ~1.05–1.2 for the latter.

[83] 5. Lateral variations in temperature and composition in the upper part of the lower mantle, in particular, appear small in comparison to those in the upper mantle.

[84] 6. A general compositional difference between the upper and the lower mantle is apparent, with the TZ possibly acting as a boundary over which the change from overall low Mg # and relatively high Mg/Si ratios to the reverse (i.e., high Mg # and low Mg/Si ratios) occurs.

[85] 7. The shear wave anisotropy structure retrieved here concurs with that found in recent whole mantle seismic tomography studies for the upper mantle, notably the strong positive shear wave anisotropy signal is clearly present. In the TZ and upper part of the lower mantle we find little evidence for  $\xi$  anisotropy.

[86] Although the use of stochastic sampling-based methods such as the Metropolis algorithm are advantageous for solving nonlinear inverse problems, they are prohibitive because of the computational costs involved. Inversion of dispersion curves for a single tectonic region will run for about 10 days on a single standard 3 GHz processor. In spite of these limitations it is our goal to increase lateral resolution to  $5^\circ \times 5^\circ$  by applying the methodology on a regional scale (e.g., the North American continent). Moreover, to further constrain the range of models compatible with surface wave data, it is also our intention to include additional data sets in the future such as gravity, electromagnetic sounding, and normal mode data.

[87] **Acknowledgments.** We are grateful for constructive reviews by S. Goes, an anonymous reviewer, and the Associate Editor. We would also like to thank J. Trampert for sharing the surface wave phase velocity maps with us. A. Zunino kindly provided Figure 1. This work was supported by the Danish agency for Science, Technology and Innovation, Swiss National Science Foundation grant 200021-130411, and partly supported by Swiss National Science Foundation grant 200021-111870.

## References

- Afonso, J. C., M. Fernández, G. Ranalli, W. L. Griffin, and J. A. D. Connolly (2008), Combined geophysical-petrological modeling of the lithospheric and sublithospheric upper mantle: Methodology and applications, *Geochem. Geophys. Geosyst.*, 9, Q05008, doi:10.1029/2007GC001834.
- Afonso, J. C., G. Ranalli, M. Fernandez, W. L. Griffin, S. Y. O'Reilly, and U. Faul (2010), On the Vp/Vs-Mg # correlation in mantle peridotites: Implications for the identification of thermal and compositional anomalies in the upper mantle, *Earth Planet. Sci. Lett.*, 289, 606.
- Anderson, D. L. (1989), *Theory of the Earth*, Blackwell, Oxford, U. K.
- Anderson, D. L., and A. M. Dziewonski (1982), Upper mantle anisotropy: Evidence from free oscillations, *Geophys. J. R. Astron. Soc.*, 69, 383.
- Anderson, D. L., and J. W. Given (1982), Absorption band  $Q$  model of the Earth, *J. Geophys. Res.*, 87, 3893.
- Anderson, D. L., and R. S. Hart (1978), Attenuation models of the Earth, *Phys. Earth Planet. Sci.*, 16, 289.
- Antolik, M., G. Ekström and A. M. Dziewonski (2001), Global event location with full and sparse datasets using three-dimensional models of mantle P-wave velocity, *Pure Appl. Geophys.*, 158, 291, doi:10.1007/PL0001161.
- Artemieva, I. M. (2006), Global  $1^\circ \times 1^\circ$  thermal model TC1 for the continental lithosphere: Implications for lithosphere secular evolution, *Tectonophysics*, 416, 245.

- Artemieva, I. M. (2009), The continental lithosphere: Reconciling thermal, seismic and petrologic data, *Lithos*, *109*, 23.
- Artemieva, I. M., and W. D. Mooney (2001), Thermal structure and evolution of Precambrian lithosphere: A global study, *J. Geophys. Res.*, *106*, 16,387.
- Babuska, V., and M. Cara (1991), *Seismic Anisotropy in the Earth*, Kluwer Acad., Boston, Mass.
- Becker, T., and L. Boschi (2002), A comparison of tomographic and geodynamic mantle models, *Geochem. Geophys. Geosyst.*, *3*(1), 1003, doi:10.1029/2001GC000168.
- Becker, T. W., B. Kustowski, and G. Ekström (2008), Radial seismic anisotropy as a constraint for upper mantle rheology, *Earth Planet. Sci. Lett.*, *267*, 213.
- Beghein, C., and J. Trampert (2003), Probability density function for radial anisotropy: Implications for the upper 1200 km of the mantle, *Earth Planet. Sci. Lett.*, *217*, 151.
- Bernardo, J. M., and A. F. M. Smith (1994), *Bayesian Theory*, John Wiley, Chichester, U. K.
- Boschi, L., and A. M. Dziewonski (1999), High and low resolution images of the Earth's mantle: Implications of different approaches to tomographic modeling, *J. Geophys. Res.*, *104*, 25,567.
- Boschi, L., and A. M. Dziewonski (2000), Whole Earth tomography from delay times of *P*, *PcP*, *PKP* phases: Lateral heterogeneities in the outer core, or radial anisotropy in the mantle?, *J. Geophys. Res.*, *105*, 13,675.
- Boschi, L., and G. Ekström (2002), New images of the Earth's upper mantle from measurements of surface-wave phase velocity anomalies, *J. Geophys. Res.*, *107*(B4), 2059, doi:10.1029/2000JB000059.
- Boschi, L., T. W. Becker, and B. Steinberger (2008), On the statistical significance of correlations between synthetic mantle plumes and tomographic models, *Phys. Earth Planet. Inter.*, *167*, 230, doi:10.1016/j.pepi.2008.03.009.
- Boyd, F. R. (1989), Compositional distinction between oceanic and cratonic lithosphere, *Earth Planet. Sci. Lett.*, *96*, 15.
- Brodholt, J., G. Helffrich, and J. Trampert (2007), Chemical versus thermal heterogeneity in the lower mantle: The most likely role of anelasticity, *Earth Planet. Sci. Lett.*, *262*, 429.
- Cammarano, F., and B. Romanowicz (2007), Insights into the nature of the transition zone from physically constrained inversion of long period seismic data, *Proc. Natl. Acad. Sci. U. S. A.*, *104*, 9139.
- Cammarano, F., B. Romanowicz, L. Stixrude, C. Lithgow-Bertelloni, and W. Xu (2009), Inferring the thermochemical structure of the upper mantle from seismic data, *Geophys. J. Int.*, *179*, 1169.
- Cobden, L., S. Goes, F. Cammarano, and J. A. D. Connolly (2008), Thermochemical interpretation of one-dimensional seismic reference models for the upper mantle: Evidence for bias due to heterogeneity, *Geophys. J. Int.*, *175*, 627.
- Cobden, L., S. Goes, M. Ravenna, E. Styles, F. Cammarano, K. Gallagher, and J. A. D. Connolly (2009), Thermochemical interpretation of 1-D seismic data for the lower mantle: The significance of nonadiabatic thermal gradients and compositional heterogeneity, *J. Geophys. Res.*, *114*, B11309, doi:10.1029/2008JB006262.
- Connolly, J. A. D. (2005), Computation of phase equilibria by linear programming: A tool for geodynamic modeling and an application to subduction zone decarbonation, *Earth Planet. Sci. Lett.*, *236*, 524.
- Debayle, E., and B. L. N. Kennett (2000), Anisotropy in the Australian upper mantle from Love and Rayleigh waveform inversion, *Earth Planet. Sci. Lett.*, *184*, 339.
- Deschamps, F., and J. Trampert (2003), Mantle tomography and its relation to composition and temperature, *Phys. Earth Planet. Inter.*, *140*, 277.
- Deschamps, F., and J. Trampert (2004), Towards a lower mantle reference temperature and composition, *Earth Planet. Sci. Lett.*, *222*, 161, doi:10.1016/j.epsl.2004.02.024.
- Deschamps, F., R. Snieder, and J. Trampert (2001), The relative density-to-shear velocity scaling in the uppermost mantle, *Phys. Earth Planet. Inter.*, *124*, 193.
- Durek, J. J., and G. Ekström (1996), A radial model of anelasticity consistent with long-period surface wave attenuation, *Bull. Seismol. Soc. Am.*, *86*, 144.
- Dziewonski, A. M. (1984), Mapping the lower mantle: Determination of lateral heterogeneity in *P* velocity up to degree and order 6, *J. Geophys. Res.*, *89*, 5929.
- Dziewonski, A. M., and D. L. Anderson (1981), Preliminary reference Earth model, *Phys. Earth Planet. Inter.*, *25*, 297.
- Dziewonski, A. M., B. H. Hager, and R. J. O'Connell (1977), Large-scale heterogeneity in the lower mantle, *J. Geophys. Res.*, *82*, 239.
- Ekström, G., and A. M. Dziewonski (1998), The unique anisotropy of the Pacific upper mantle, *Nature*, *394*, 168.
- Ekström, G., J. Tromp, and E. W. F. Larson (1997), Measurements and global models of surface wave propagation, *J. Geophys. Res.*, *102*, 8137.
- Faul, U. H., and I. Jackson (2005), The seismological signature of temperature and grain size variations in the upper mantle, *Earth Planet. Sci. Lett.*, *234*, 119.
- Forté, A. M., and J. X. Mitrovica (2001), Deep-mantle high-viscosity flow and thermochemical structure inferred from seismic and geodynamic data, *Nature*, *410*, 1049.
- Forté, A. M., and C. A. Perry (2000), Seismic-geodynamic evidence for a chemically depleted continental tectosphere, *Science*, *290*, 1940.
- Forté, A. M., R. L. Woodward and A. M. Dziewonski (1994), Joint inversion of seismic and geodynamic data for models of three-dimensional mantle heterogeneity, *J. Geophys. Res.*, *99*, 21,857.
- Gaul, O. F., W. L. Griffin, S. Y. O'Reilly, and N. J. Pearson (2000), Mapping olivine composition in the lithospheric mantle, *Earth Planet. Sci. Lett.*, *182*, 223.
- Godey, S., F. Deschamps, J. Trampert, and R. Snieder (2004), Thermal and compositional anomalies beneath the North American continent, *J. Geophys. Res.*, *109*, B01308, doi:10.1029/2002JB002263.
- Goes, S., and S. van der Lee (2002), Thermal structure of the North American uppermost mantle inferred from seismic tomography, *J. Geophys. Res.*, *107*(B3), 2050, doi:10.1029/2000JB000049.
- Goes, S., R. Govers, and P. Vacher (2000), Shallow mantle temperatures under Europe from *P* and *S* wave tomography, *J. Geophys. Res.*, *105*, 11,153.
- Goes, S., F. J. Simons, and K. Yoshizawa (2005), Seismic constraints on temperature of the Australian uppermost mantle, *Earth Planet. Sci. Lett.*, *236*, 227.
- Griffin, W. L., et al. (1999), Layered mantle lithosphere in the Lac du Gras Area, Slave Craton: Composition, structure and origin, *J. Petrol.*, *40*, 705.
- Gudmundsson, O., and M. Sambridge (1998), A regionalized upper mantle (RUM) seismic model, *J. Geophys. Res.*, *103*, 7121.
- Gung, Y. M. Panning, and B. Romanowicz (2003), Global anisotropy and the thickness of continents, *Nature*, *442*, 707.
- Hart, S. R., and A. Zindler (1986), In search of a bulk-Earth composition, *Chem. Geol.*, *57*, 247.
- Irfune, T. (1994), Absence of an aluminous phase in the upper part of the Earth's lower mantle, *Nature*, *370*, 131.
- Ishii, M., and J. Tromp (2001), Even-degree lateral variations in the mantle constrained by free oscillations and the free-air gravity anomaly, *Geophys. J. Int.*, *145*, 77.
- Ishii, M., and J. Tromp (2004), Constraining large-scale mantle heterogeneity using mantle and inner-core sensitive normal modes, *Phys. Earth Planet. Inter.*, *146*, 113.
- Jackson, I. (1998), Elasticity, composition and the temperature of the Earth's lower mantle: A reappraisal, *Geophys. J. Int.*, *134*, 291.
- Jackson, I. (2000), Laboratory measurements of seismic wave dispersion and attenuation: Recent progress, in *Earth's Deep Interior: Mineral Physics and Tomography from the Atomic to the Global Scale*, *Geophys. Monogr. Ser.*, vol. 117, edited by S. Karato et al., p. 265, AGU, Washington, D. C.
- Jackson, I., J. D. Fitz Gerald, U. H. Faul, and B. H. Tan (2002), Grain-size-sensitive seismic wave attenuation in polycrystalline olivine, *J. Geophys. Res.*, *107*(B12), 2360, doi:10.1029/2001JB001225.
- Jaupart, C., and J.-C. Mareschal (1999), Thermal structure and thickness of continental roots, *Lithos*, *48*, 93.
- Jordan, T. H. (1978), Composition and development of the continental tectosphere, *Nature*, *274*, 544.
- Jordan, T. H. (1981), Global tectonic regionalization for seismological data analysis, *Bull. Seismol. Soc. Am.*, *71*, 1131.
- Kanamori, H., and D. L. Anderson (1977), Importance of physical dispersion in surface wave and free oscillation problems, *Rev. Geophys.*, *15*, 105.
- Karato, S.-I. (1993), Importance of anelasticity in the interpretation of seismic tomography, *Geophys. Res. Lett.*, *20*, 1623.
- Karato, S.-I. (1998), Seismic anisotropy in the deep mantle, boundary layers and the geometry of mantle convection, *Pure Appl. Geophys.*, *151*, 565.
- Karato, S.-I., and H. Spetzler (1990), Defect microdynamics in minerals and solid state mechanisms of seismic wave attenuation and velocity dispersion in the mantle, *Rev. Geophys.*, *28*, 399.
- Kennett, B. L. N. (2006), On seismological reference models and the perceived nature of heterogeneity, *Phys. Earth Planet. Inter.*, *159*, 129.
- Kennett, B. L. N., E. R. Engdahl, and R. Buland (1995), Constraints on seismic velocities in the Earth from travel times, *Geophys. J. Int.*, *122*, 108.
- Khan, A., J. A. D. Connolly, J. MacLennan, and K. Mosegaard (2007), Joint inversion of seismic and gravity data for lunar composition and thermal state, *Geophys. J. Int.*, *168*, 243, doi:10.1111/j.1365-246X.2006.03200.x.
- Khan, A., J. A. D. Connolly, and S. R. Taylor (2008), Inversion of seismic and geodetic data for the major element chemistry and temperature of the Earth's mantle, *J. Geophys. Res.*, *113*, B09308, doi:10.1029/2007JB005239.

- Khan, A., L. Boschi, and J. A. D. Connolly (2009), On mantle chemical and thermal heterogeneities and anisotropy as mapped by inversion of global surface wave data, *J. Geophys. Res.*, *114*, B09305, doi:10.1029/2009JB006399.
- Kuo, C., and B. Romanowicz (2000), On the resolution of density anomalies in the Earth's mantle using spectral fitting of normal mode data, *Geophys. J. Int.*, *150*, 162.
- Kuskov, O. L., V. A. Kronrod, and H. Annersten (2006), Upper mantle temperatures from seismic and geochemical constraints: Implications for the Kaapvaal craton, *Earth Planet. Sci. Lett.*, *244*, 133, doi:10.1016/j.epsl.2006.02.016.
- Kustowski, B. (2007), Modelling the anisotropic shear-wave velocity structure in the Earth's mantle on global and regional scales, Ph.D. thesis, Harvard Univ., Cambridge, Mass.
- Kustowski, B., G. Ekström, and A. M. Dziewonski (2008), Anisotropic shear-wave velocity structure of the Earth's mantle: A global model, *J. Geophys. Res.*, *113*, B06306, doi:10.1029/2007JB005169.
- Lawrence, J. F., and M. E. Wysession (2006), QLM9: A new radial quality factor ( $Q\mu$ ) model for the lower mantle, *Earth Planet. Sci. Lett.*, *241*, 962, doi:10.1016/j.epsl.2005.10.030.
- Lebedev, S., and R. D. van der Hilst (2008), Global upper-mantle tomography with the automated multimode inversion of surface and  $S$ -wave forms, *Geophys. J. Int.*, *173*, 505.
- Lebedev, S., T. Meier, and R. D. van der Hilst (2006), Asthenospheric flow and origin of volcanism in the Baikal Rift area, *Earth Planet. Sci. Lett.*, *249*, 415.
- Lebedev, S., J. Boonen, and J. Trampert (2009), Seismic structure of Precambrian lithosphere: New constraints from broad-band surface-wave dispersion, *Lithos*, *109*, 96.
- Lyubetskaya, T., and J. Korenaga (2007), Chemical composition of Earth's primitive mantle and its variance: 1. Method and results, *J. Geophys. Res.*, *112*, B03211, doi:10.1029/2005JB004223.
- Marone, F., Y. Gung, and B. Romanowicz (2006), Three-dimensional radial anisotropic structure of the North American upper mantle from the inversion of surface waveform data, *Geophys. J. Int.*, *171*, 206, doi:10.1111/j.1365-246X.2007.03465.
- Masters, G., G. Laske, H. Bolton, and A. M. Dziewonski (2000), The relative behaviour of shear velocity, bulk sound speed, and compressional velocity in the mantle: Implications for chemical and thermal structure, in *Earth's Deep Interior: Mineral Physics and Tomography From the Atlantic to the Global Scale*, *Geophys. Monogr. Ser.*, vol. 117, edited by S. Karato et al., p. 63, AGU, Washington, D. C.
- Matas, J., and M. S. T. Bukowinski (2007), On the anelastic contribution to the temperature dependence of lower mantle seismic velocities, *Earth Planet. Sci. Lett.*, *259*, 51.
- McDonough, W. F., and S. S. Sun (1995), The composition of the Earth, *Chem. Geol.*, *120*(3–4), 223.
- McKenzie, D. P., J. A. Jackson, and K. F. Priestley (2005), Thermal structure of oceanic and continental lithosphere, *Earth Planet. Sci. Lett.*, *233*, 337.
- Minster, B., and D. L. Anderson (1981), A model of dislocation controlled rheology for the mantle, *Philos. Trans. R. Soc. London, Ser. A*, *299*, 319.
- Montagner, J. P. (1994), Can seismology tell us anything about convection in the mantle?, *Rev. Geophys.*, *32*, 115.
- Montagner, J. P. (1998), Where can seismic anisotropy be detected in the Earth's mantle? *Pure Appl. Geophys.*, *151*, 223.
- Montagner, J. P., and B. L. N. Kennett (1996), How to reconcile body-wave and normal-mode reference Earth models, *Geophys. J. Int.*, *125*, 229.
- Montagner, J. P. and T. Tanimoto (1991), Global upper mantle tomography of seismic velocities and anisotropies, *J. Geophys. Res.*, *96*, 20,337.
- Mosegaard, K., and M. Sambridge (2002), Monte Carlo analysis of inverse problems, *Inverse Probl.*, *18*, R29, doi:10.1088/0266-5611/18/3/201.
- Mosegaard, K., and A. Tarantola (1995), Monte Carlo sampling of solutions to inverse problems, *J. Geophys. Res.*, *100*, 12,431.
- Nataf, H.-C., and Y. Ricard (1996), 3SMAC: An a priori tomographic model of the upper mantle based on geophysical modelling, *Phys. Earth Planet. Inter.*, *95*, 101.
- Nettles, M., and A. M. Dziewonski (2008), Radially anisotropic shear-velocity structure of the upper mantle globally and beneath North America, *J. Geophys. Res.*, *113*, B02303, doi:10.1029/2006JB004819.
- Nolet, G., S. P. Grand, and B. L. N. Kennett (1994), Seismic heterogeneity in the upper mantle, *J. Geophys. Res.*, *99*, 23,753.
- Palme, H., and H. St. C. O'Neill (2003), Cosmochemical estimates of mantle composition, in *Treatise on Geochemistry*, edited by H. D. Holland and K. H. Turekian, p. 1, Elsevier, New York.
- Panning, M., and B. Romanowicz (2006), A three-dimensional radially anisotropic model of shear velocity in the whole mantle, *Geophys. J. Int.*, *167*, 361.
- Priestley, K. F., and D. P. McKenzie (2006), The thermal structure of the lithosphere from shear wave velocities, *Earth Planet. Sci. Lett.*, *244*, 285.
- Rawlinson, N., S. Pozgay, and S. Fishwick (2010), Seismic tomography: A window into deep Earth, *Phys. Earth Planet. Inter.*, *178*, 101.
- Resovsky, J., and M. H. Ritzwoller (1999), Regularization uncertainty in density model estimated from normal mode data, *Geophys. Res. Lett.*, *26*, 2319.
- Resovsky, J., and J. Trampert (2003), Using probabilistic seismic tomography to test mantle velocity-density relationships, *Earth Planet. Sci. Lett.*, *215*, 121.
- Ringwood, A. E. (1975), *Composition and Petrology of the Earth's Mantle*, McGraw-Hill, New York.
- Ritsema, J., H. J. Van Heijst, and J. H. Woodhouse (2004), Global transition zone tomography, *J. Geophys. Res.*, *109*, B02302, doi:10.1029/2003JB002610.
- Ritsema, J., W. Xu, L. Stixrude, and C. Lithgow-Bertelloni (2009), Estimates of the transition zone temperature in a mechanically mixed upper mantle, *Earth Planet. Sci. Lett.*, *277*, 244, doi:10.1016/j.epsl.2008.10.024.
- Ritzwoller, M. H., and E. M. Lavelly (1995), Three-dimensional seismic models of the Earth's mantle, *Rev. Geophys.*, *33*, 1.
- Ritzwoller, M. H., N. M. Shapiro, and S.-J. Zhong (2004), Cooling history of the Pacific lithosphere, *Earth Planet. Sci. Lett.*, *226*, 69.
- Robertson, G. S., and J. H. Woodhouse (1996), Ratio of relative  $S$  to  $P$  heterogeneity in the lower mantle, *J. Geophys. Res.*, *101*, 20,041.
- Röhm, A. H. E., R. Snieder, S. Goes, and J. Trampert (2000), Thermal structure of continental upper mantle inferred from  $S$ -wave velocity and surface heat flow, *Earth Planet. Sci. Lett.*, *181*, 395.
- Romanowicz, B. (2001), Can we resolve 3D density heterogeneity in the lower mantle?, *Geophys. Res. Lett.*, *28*, 1107.
- Romanowicz, B. (2003), Global mantle tomography: Progress status in the past 10 years, *Annu. Rev. Earth Planet. Sci.*, *31*, 303.
- Romanowicz, B., and B. Mitchell (2007), Deep Earth structure: Q of the Earth from crust to core, in *Treatise on Geophysics*, vol. 1, edited by G. Schubert, p. 731, Elsevier, Amsterdam.
- Rudnick, R. L., W. F. McDonough, and R. J. O'Connell (1998), Thermal structure, thickness and composition of continental lithosphere, *Chem. Geol.*, *145*, 395.
- Saltzer, R. L., R. H. van der Hilst, and H. Karason (2001), Comparing  $P$  and  $S$  wave heterogeneity in the mantle, *Geophys. Res. Lett.*, *28*, 1335.
- Sambridge, M., and K. Mosegaard (2002), Monte Carlo methods in geophysical inverse problems, *Rev. Geophys.*, *40*(3), 1009, doi:10.1029/2000RG000089.
- Sebai, A., E. Stutzmann, and J. P. Montagner (2006), Anisotropic structure of the African upper mantle structure from Rayleigh and Love wave tomography, *Phys. Earth Planet. Inter.*, *155*, 48.
- Shapiro, N. M., and M. H. Ritzwoller (2002), Monte-Carlo inversion for a global shear-velocity model of the crust and upper mantle, *Geophys. J. Int.*, *151*, 88.
- Shapiro, N. M., and M. H. Ritzwoller (2004), Thermodynamic constraints on seismic inversions, *Geophys. J. Int.*, *157*, 1175, doi:10.1111/j.1365-246X.2004.02254.x.
- Simmons, N. A., A. M. Forte, and S. P. Grand (2009), Joint seismic, geodynamic and mineral physical constraints on three-dimensional mantle heterogeneity: Implications for the relative importance of thermal versus compositional heterogeneity, *Geophys. J. Int.*, *177*, 1284.
- Simons, F. J., A. Zielhuis, and R. D. van der Hilst (1999), The deep structure of the Australian continent from surface-wave tomography, *Lithos*, *48*, 17.
- Sobolev, S. V., et al. (1996), Upper mantle temperatures from teleseismic tomography of French Massif Central including effects of composition, mineral reactions, anharmonicity, anelasticity and partial melt, *Earth Planet. Sci. Lett.*, *157*, 193.
- Stein, C. A., and S. Stein (1992), A model for the global variation in oceanic depth and heat flow with lithospheric age, *Nature*, *359*, 123.
- Stixrude, L., and C. Lithgow-Bertelloni (2005), Mineralogy and elasticity of the oceanic upper mantle: Origin of the low-velocity zone, *J. Geophys. Res.*, *110*, B03204, doi:10.1029/2004JB002965.
- Su, W. J., and A. M. Dziewonski (1997), Simultaneous inversion for 3-D variations in shear and bulk velocity in the mantle, *Phys. Earth Planet. Inter.*, *101*, 135.
- Tanimoto, T., and D. L. Anderson (1984), Mapping convection in the mantle, *Geophys. Res. Lett.*, *11*, 287.
- Tarantola, A., and B. Valette (1982), Inverse problems: Quest for information, *J. Geophys.*, *50*, 159.
- Taylor, S. R. (1980), Refractory and moderately volatile element abundances in the Earth, Moon and meteorites, *Proc. Lunar Planet. Sci. Conf.*, *11*, 333.
- Trampert, J. (1998), Global seismic tomography: The inverse problem and beyond, *Inverse Probl.*, *14*, 371, doi:10.1088/0266-5611/14/3/002.

- Trampert, J., and R. D. van der Hilst (2005), Towards a quantitative interpretation of global seismic tomography, in *Earth's Deep Mantle: Structure, Composition and Evolution*, *Geophys. Monogr. Ser.*, vol. 160, edited by R. D. van der Hilst et al., p. 47, AGU, Washington, D. C.
- Trampert, J., and J. H. Van Heijst (2002), Global azimuthal anisotropy in the transition zone, *Science*, *296*, 1297, doi:10.1126/science.1070264.
- Trampert, J., and J. H. Woodhouse (2001), Assessment of global phase velocities, *Geophys. J. Int.*, *144*, 165.
- Trampert, J., F. Deschamps, J. Resovsky, and D. Yuen (2004), Chemical heterogeneities throughout the lower mantle, *Science*, *306*, 853.
- Verhoeven, O., A. Mocquet, P. Vacher, A. Rivoldini, M. Menvielle, P.-A. Arrial, G. Choblet, P. Tarits, V. Dehant, and T. Van Hoolst (2009), Constraints on thermal state and composition of the Earth's lower mantle from electromagnetic impedances and seismic data, *J. Geophys. Res.*, *114*, B03302, doi:10.1029/2008JB005678.
- Visser, K., J. Trampert, and B. L. N. Kennett (2008a), Global anisotropic phase-velocity maps for higher mode Love and Rayleigh waves, *Geophys. J. Int.*, *172*, 1016.
- Visser, K., J. Trampert, S. Lebedev, and B. L. N. Kennett (2008b), Probability of radial anisotropy in the deep mantle, *Earth Planet. Sci. Lett.*, *270*, 241, doi:10.1016/j.epsl.2008.03.041.
- Widmer, R., G. Masters, and F. Gilbert (1991), Spherically symmetric attenuation within the Earth from normal mode data, *Geophys. J. Int.*, *104*, 541.
- Woodhouse, J. H., and A. M. Dziewonski (1984), Mapping the upper mantle: Three-dimensional modeling of Earth structure by inversion of seismic waveforms, *J. Geophys. Res.*, *89*, 5953.
- Wookey, J., J.-M. Kendall, and G. Barruol (2002), Mid-mantle deformation inferred from seismic anisotropy, *Nature*, *415*, 777.
- Xu, W., C. Lithgow-Bertelloni, L. Stixrude, and J. Ritsema (2008), The effect of bulk composition and temperature on mantle seismic structure, *Earth Planet. Sci. Lett.*, *275*, 70, doi:10.1016/j.epsl.2008.08.012.
- Yoshizawa, K., and B. L. N. Kennett (2004), Multimode surface wave tomography for the Australian region using a three-stage approach incorporating finite frequency effects, *J. Geophys. Res.*, *109*, B02310, doi:10.1029/2002JB002254.
- Zielhuis, A., and G. Nolet (1994), Shear wave velocity variations in the upper mantle under central Europe, *Geophys. J. Int.*, *117*, 695.

---

L. Boschi, Institute of Geophysics, Swiss Federal Institute of Technology, Sonneggstr. 5, CH-8092 Zurich, Switzerland. (larryboschi@gmail.com)

J. A. D. Connolly and A. Khan, Institute of Geochemistry and Petrology, Swiss Federal Institute of Technology, Clausiusstr. 25, CH-8092 Zurich, Switzerland. (james.connolly@erdw.ethz.ch; amir@erdw.ethz.ch)